CDK4/6 inhibition induces a DNA damage-independent senescence-associated secretory phenotype driven by delayed activation of NF-κB

Joanna Lan-Hing Yeung[1,*], Justin Rendleman[1,*], Lauren Anderson Westcott[1], Arnold Ou[1], Matthew Pressler[1], Nicole Pagane[1], Irene Duba[1], Ria Hosuru[1], Bat-Ider Tumenbayar[1], Viviana I. Risca[1]

[1]Laboratory of Genome Architecture and Dynamics, The Rockefeller University, New York, NY 10065, USA.

*These authors contributed equally

Correspondence: vrisca@rockefeller.edu

ABSTRACT

Cellular senescence consists of regulated cell phenotypes associated with permanent exit from the cell cycle in response to stressors such as genomic instability. The consequences of senescence go beyond individual cells due to the senescence associated secretory phenotype (SASP), which can induce inflammation in neighboring cells. Some cancers respond to CDK4/6 inhibitors (CDK4/6i)—a family of targeted therapies that inhibit proliferation—with a senescence-like phenotype in the absence of DNA damage. We asked how the SASP and the transcriptional regulatory profile triggered by CDK4/6i-driven arrest compares to the canonical NF-κB-regulated SASP triggered by DNA damage. We profiled the temporal dynamics of transcriptional regulation in response to the CDK4/6i, palbociclib, and the DNA damaging agent, doxorubicin. We found that, although upregulation of NF-κB driven-SASP genes is shared across both drugs, it is delayed in CDK4/6i. This coincides with slower enhancer activation and epigenetic changes. Interestingly, ATM/ATR inhibition does not affect CDK4/6i-induced NF-κB nuclear localization, pointing to an alternative mechanism driving NF-κB activity in the absence of DNA damage. Inhibiting NF-κB suppresses the expression of shared SASP genes without reversing stable arrest. This points to SASP manipulation as a potential therapeutic strategy, and resolves an ongoing controversy about the nature of cell cycle arrest-driven SASP.

INTRODUCTION

Cellular senescence is a state of stable cell cycle arrest that suppresses tumorigenesis by limiting the proliferation of cells that are aged, damaged, or stressed (Ajoolabady et al. 2025). However, even in established tumors, certain therapeutics can force cancer cells into therapy-induced senescence and thereby curb tumor growth (Schmitt et al. 2022). While DNA damage has historically been considered a requirement for entry into senescence, emerging targeted therapies can induce senescent-like states outside of DNA damaging agents and radiation; these include inhibitors of the cyclin-dependent kinases CDK4 and CDK6 (CDK4/6i) (Kovatcheva et al. 2017; Klein et al. 2018; Wagner and Gil 2020). An outstanding question in the field is whether senescence, when caused by dramatically different triggers, converges on a common cell state, or represents a heterogeneous set of states sharing core phenotypic qualities. It is imperative to understand the molecular mechanisms underlying distinct growth-arrest states, as regulatory networks intrinsic to normal aging and stress responses can ultimately shape therapeutic outcomes (Lee and Schmitt 2019; Schmitt et al. 2022; Gleason et al. 2024).

Although senescent cells can no longer divide, they remain metabolically active and acquire features that continually evolve (Schmitt et al. 2022). As such, no universal biomarker of senescence exists, and identification of senescent cells relies on the characterization of several hallmarks (Hernandez-Segura et al. 2018). Beyond stable growth arrest, senescent cells exhibit enlarged morphology, heightened lysosomal content to maintain homeostasis in stressed conditions, increased nuclear size, as well as extensive alterations in the chromatin landscape, including senescence-associated heterochromatic foci (SAHFs) (Hernandez-Segura et al. 2018). Importantly, senescent

53 cells secrete a complex network of cytokines and chemokines, along with other
54 bioactive factors, known as the senescence-associated secretory phenotype (SASP)
55 (Wang et al. 2024); this process increases the paracrine signaling of these “dormant”
56 cells, thus imbuing them with significant influence over the neighboring environment.

57 Given its effects on the tumor microenvironment, identifying regulators of the SASP
58 across distinct therapeutic triggers of senescence is critical for understanding its impact
59 on disease outcomes. The SASP acts as a double-edged sword, having pro- and anti-
60 tumorigenic effects, depending on its composition (Lau and David 2019). The benefits of
61 the SASP include reinforcing stable arrest through both autocrine and paracrine signals,
62 while facilitating a robust anti-tumor immune response. In contrast, a chronic pro-
63 inflammatory SASP drives increased invasive and migratory capacity of cancer cells,
64 promoting angiogenesis and immune evasion (Schmitt et al. 2022).

65 The regulation and composition of the SASP have largely been investigated in model
66 systems in which senescence is induced by DNA damage or genome instability (Rodier
67 et al. 2009; Malaquin et al. 2016). Such triggers have been shown to induce expression
68 of inflammatory genes through stimulation of NF-κB, a master regulator of the SASP
69 (Chien et al. 2011b); this is coordinated via the DNA damage response kinase, ATM
70 (Miyamoto 2011; Bournique et al. 2025). While DNA damaging agents are frequently
71 applied in cancer therapeutic approaches, targeted therapies like CDK4/6i can induce
72 senescent-like states through non-DNA damage mechanisms. This begs the question,
73 what drives the SASP when there is cellular senescence but not DNA damage? Prior
74 studies of the response to CDK4/6i treatment have thus far offered conflicting results

75 regarding the involvement of NF-κB (Goel et al. 2017; Guan et al. 2017; Wang et al.
76 2022; Gleason et al. 2024; Lee et al. 2024).

77 Here we sought to investigate: (1) does the presence (or absence) of DNA damage give
78 rise to distinct therapy-induced senescent cell states and SASP profiles over time? and
79 (2) what epigenetic changes dynamically regulate the SASP in cancer cells in response
80 to therapeutics? We chose to address these questions systematically in a liposarcoma
81 model, a rare type of malignant mesenchymal tumor with limited treatment options in
82 advanced disease. Over 90% of liposarcoma tumors are characterized by co-
83 amplification of *CDK4* and *MDM2* (Creytens et al. 2015), and previous work has shown
84 that CDK4/6i can induce a full senescence program with irreversible arrest driven by
85 *ANGPTL4*, correlating with patient outcomes and clinical efficacy (Kovatcheva et al.
86 2015; Dickson et al. 2016; Gleason et al. 2024). While traditional chemotherapeutics,
87 such as doxorubicin, trigger senescence through DNA damage, CDK4/6i instead arrest
88 cells in G1 by preventing the activity of E2F transcription factors in a DNA damage-
89 independent mechanism (Guan et al. 2017; Kovatcheva et al. 2017; Gleason et al.
90 2024) (Fig. 1A). We performed an extended 28-day time course directly comparing
91 these two distinct triggers of therapy-induced senescence. By profiling epigenomic
92 changes across multiple time points, we captured the temporal evolution of
93 senescence-associated gene regulatory programs, including features that would be
94 missed in short-term studies.

95 We find that early senescence programs are trigger-specific and largely remain distinct,
96 including p53 activation following doxorubicin-induced DNA damage and an
97 extracellular matrix (ECM)-enriched SASP program upon CDK4/6i treatment. At later

98 time points, both therapies initiate a shared NF-κB-driven SASP, albeit with slower
99 induction in the absence of DNA damage. Such activation of NF-κB is conserved
100 beyond liposarcoma, observing a similar response in breast cancer cells. By extending
101 the duration of CDK4/6i treatment here, we revealed delayed NF-κB activation and
102 clarify its previously debated role from short-term studies, where its activity was not
103 detected. Notably, NF-κB inhibition suppresses the shared SASP without reversing
104 stable arrest, suggesting that selective modulation of SASP composition is possible
105 while preserving growth arrest, representing new therapeutic opportunities to explore.

106 RESULTS

107 CDK4/6i and doxorubicin both induce senescence features with distinct levels of
108 DNA damage and p53 activation

109 To understand whether the absence or presence of DNA damage drives distinct cell
110 states over time, we compared 1 μM palbociclib (Palbo), a type of CDK4/6i, against 100
111 nM doxorubicin (Doxo), standard chemotherapy, over a 28-day period across multiple
112 timepoints in a patient-derived dedifferentiated liposarcoma cell line, LS8817 (Singer et
113 al. 2007; Brill et al. 2010; Crago and Singer 2011) (Fig. 1B). Among multiple well-
114 differentiated/dedifferentiated liposarcoma (WD/DDLS) cell lines tested, LS8817 was
115 among those which undergoes stable senescence in response to palbociclib
116 (Kovatcheva et al. 2015; Kovatcheva et al. 2017), providing a unique and experimentally
117 tractable system for interrogating CDK4/6i-induced senescence in a clinically relevant
118 cancer type. To investigate the full breadth of gene regulatory networks that underlie the
119 senescent state, we performed a time-resolved, multi-omics analysis that profiles the

120 transcriptome using mRNA-seq, accessible chromatin regions by ATAC-seq, and the
121 epigenome using CUT&Tag and CUT&RUN methods (Fig. 1B; Supplemental Table 1).

122 We first validated that cells are entering into a senescent state in response to both drug
123 treatments. Since there is no universal biomarker of senescence, we measured several
124 accepted hallmarks of senescence. We observed an increased amount of lysosomal
125 activity, through senescence-associated beta galactosidase (SA-βgal) staining, in both
126 CDK4/6i and doxorubicin over time (Fig. 1C). We confirmed cells entered a stable
127 growth arrest state by assessing for clonogenic outgrowth upon drug removal (Fig. 1D).
128 In these clonogenic outgrowth assays, doxorubicin caused a stable arrest in nearly the
129 entire population early in treatment, by day 3, whereas stable arrest did not occur for
130 most cells in response to palbociclib until day 14 of treatment (Fig. 1D). We also
131 measured senescence-associated nuclear changes by immunofluorescence staining for
132 the heterochromatin remodeler, ATRX (Kovatcheva et al. 2015; Kovatcheva et al. 2017)
133 and the histone variant, macroH2A, a key structural SAHF component (Zhang et al.
134 2005) (Fig. 1E, F). Indeed, we saw that both treatments lead to an accumulation of both
135 ATRX foci and SAHFs (Fig. 1E,F), indicating that the global chromatin landscape does
136 undergo dynamic changes during senescence.

137 Given the differences in the mechanisms of action for each drug, we anticipated the
138 amount of DNA damage would be a distinctive feature between treatments. We
139 measured the foci of γH2AX, a classical marker of DNA damage, and 53BP1, a DNA
140 repair factor (Fig. 1G,H). We found that even by day 28 of palbociclib treatment, the
141 amount of DNA damage-associated foci remains comparable to that of untreated cycling
142 controls (Fig. 1G). This contrasts with doxorubicin treatment, under which DNA damage

143 is robustly induced and remains elevated across all timepoints (Fig. 1G). Next, we
144 asked whether these differences in DNA damage are also reflected in the levels of
145 phosphorylated p53, indicative of activation of the downstream DNA damage response
146 (Sakaguchi et al. 1998; Saito et al. 2002; Loughery et al. 2014). Immunoblotting for
147 phosphorylated p53 (Serine 15) and total p53 protein levels confirmed that CDK4/6i
148 treatment does not result in downstream activation of p53, whereas p53 is robustly
149 activated in doxorubicin (Fig. 1I). Thus, our results demonstrate that CDK4/6i treatment
150 can induce senescence without the requirement for persistent DNA damage or
151 activation of the DNA damage response.

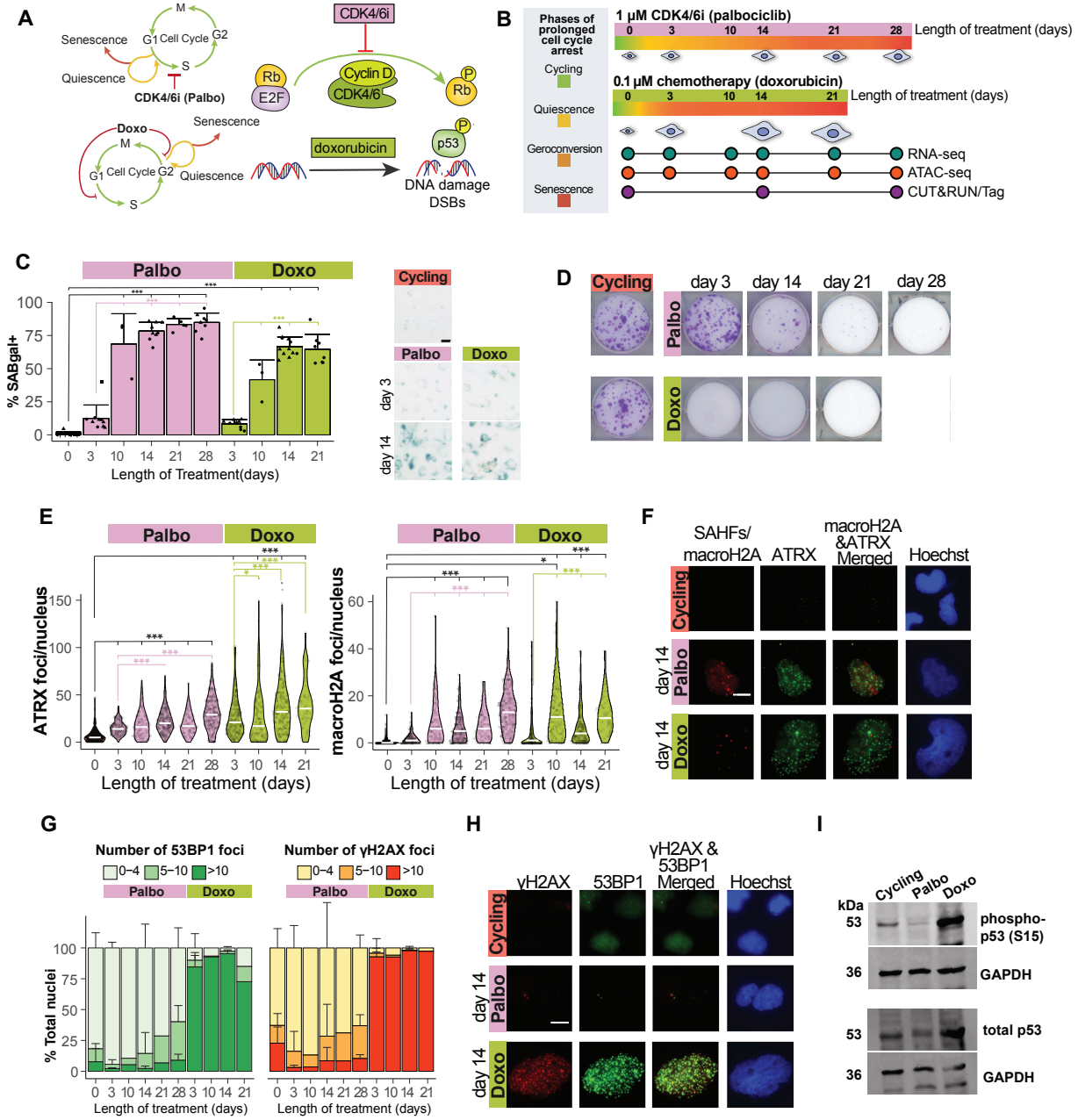
A
Senescence
Quiescence
CDK4/6i (Palbo)
Cell Cycle
CDK4/6i
Rb
E2F
Cyclin D
CDK4/6
Doxo
doxorubicin
p53
DNA damage
DSBs
B
Phases of prolonged cell cycle arrest
Cycling
Quiescence
Geroconversion
Senescence
1 μM CDK4/6i (palbociclib)
Length of treatment (days)
0.1 μM chemotherapy (doxorubicin)
RNA-seq
ATAC-seq
CUT&RUN/Tag
C
Palbo
Doxo
% SABgal+
Length of Treatment(days)
Cycling
day 3
day 14
D
day 3
day 14
day 21
day 28
E
ATRX foci/nucleus
macroH2A foci/nucleus
Length of treatment (days)
F
SAHFs/ macroH2A
ATRX
macroH2A &ATRX Merged
Hoechst
G
Number of 53BP1 foci
Number of γH2AX foci
0–4
5–10
>10
% Total nuclei
H
γH2AX
53BP1
γH2AX & 53BP1 Merged
I
kDa
phospho-p53 (S15)
GAPDH
total p53

152

153

Fig. 1: CDK4/6i and doxorubicin both induce senescence features with distinct levels of DNA damage and p53 activation

A. Diagram summarizing CDK4/6i (Palbo) vs. doxorubicin (Doxo) mechanisms of cell cycle arrest.
B. Schematic overview of comparative time-course between CDK4/6i and doxorubicin and multi-omics approaches used to profile the transcriptome (RNA-seq), chromatin accessibility (ATAC-seq) and epigenome (CUT&RUN/Tag) in LS8817 cells. At least 2 biological replicates per timepoint and drug treatment were profiled.
C. Left: Percent nuclei counted that had cellular SA-βgal+ staining at different timepoints. Number of nuclei counted was > 300 per condition at 10x objective magnification. Each point represents a field of view, with different shapes indicating biological replicates. Error bars denote standard deviation. Right: Representative SA-βgal staining images at day 3 and day 14 shown at 10x objective magnification with scale bar = 50 μm.
D. Crystal violet staining after clonogenic outgrowth for 10-12 days. 800 cells were seeded per well in a 6-well plate in drug-free media after completion of drug treatment at each timepoint.
E. Number of ATRX foci (left) and macroH2A foci (indicative of SAHFs; right) per nucleus was counted for ~100 nuclei per timepoint.
F. Representative ATRX and SAHF images are shown at day 14 of each drug treatment at 60x objective magnification. The scale bar is 15 μm.
G. Number of γH2AX foci and 53BP1 foci per nucleus was counted for ~100 nuclei per timepoint and stratified into 0-4, 5-10 or >10 foci/nuclei.
H. Representative images of γH2AX and 53BP1 staining are shown at day 14 of each drug treatment at 60x objective magnification. The scale bar is 15 μm.
I. Western blots of Serine 15-phosphorylated p53 (phospho-p53) and total p53 in Cycling, Palbo- and Doxo-treated LS8817 cell lysates harvested 18 days after treatment started. GAPDH was used as a loading control. Samples are from a separate experiment, independent of multi-omics data.

183 **Global changes in the epigenome and transcriptome define drug-induced**
184 **senescence trajectories**

185 Given that both treatments drive cells into a senescent state, we asked whether the
186 overall transcriptional regulatory state of these cells depends on the driver, particularly
187 since doxorubicin triggers DNA damage while palbociclib does not. We assayed the
188 regulatory landscape with ATAC-seq to measure chromatin accessibility. Sample
189 distance measures and principal component analysis showed that the global
190 transcriptome and chromatin accessibility landscape continues to change throughout
191 senescence (Supplemental Fig. 1A). These overall changes correspond to the timing of
192 the stable growth arrest state as observed by accumulation of SA-βgal and reduced
193 clonogenic outgrowth (Fig. 1C,D).

194 We found that many changes in chromatin accessibility trended in the same direction,
195 but the timing and magnitude of the change was often dependent on the treatment (Fig.
196 2A). A common feature among the senescent cells was decreased accessibility proximal
197 to promoters (Fig. 2B: top). These regions are enriched in E2F motifs (Supplemental
198 Fig. 1C,D), and thus their repression is indicative of cells disengaged from active
199 cycling. Increases in accessibility, on the other hand, were predominantly localized to
200 intergenic and intronic regions (Fig. 2B: bottom), suggesting potential enhancer
201 activation. These regions are enriched for motifs of stress-responsive and lineage-
202 specifying transcription factors (Balamurugan and Sterneck 2013; Kamachi and Kondoh
203 2013; Sarkar and Hochedlinger 2013; Golson and Kaestner 2016; Tremblay et al. 2018;
204 Huh et al. 2019; Romano and Miccio 2020; Awasthi et al. 2021; Currey et al. 2021; Li et
205 al. 2023; Ren et al. 2023) (Supplemental Fig. 1E), consistent with activation of

206 transcriptional programs that shape senescence-associated cell fate decisions beyond
207 cell cycle arrest.

208 We wondered whether enhancer activation dynamics differ depending on the timing of
209 senescence entry; to capture these changes, we profiled H3K27ac, a histone mark of
210 active enhancers. We found that 28% of all peaks that increased in accessibility also
211 displayed significantly increased H3K27ac signal (Supplemental Fig. 1F), indicating
212 remodeling of the enhancer landscape underlying the therapy-induced senescent state.
213 Accordingly, we defined these regions as drug-activated enhancers (Fig. 2C).
214 Somewhat surprisingly, the majority of these activated enhancer elements were shared
215 across treatment, albeit with different dynamics (Fig. 2C). H3K27ac in shared-
216 upregulated enhancers gradually increases with CDK4/6i treatment, reaching levels
217 similar to that of day 14 doxorubicin by day 28 (Fig. 2C). This is supported by principal
218 component analysis, which shows that day 28 palbociclib clusters more closely with day
219 14 doxorubicin than day 14 palbociclib (Supplemental Fig. 1G). This delayed enhancer
220 activation in the CDK4/6i treated cells corresponds to slower progression into stable
221 growth arrest (Fig. 1D).

222 We next asked how the transcriptional landscape compared between these two distinct
223 therapy-induced senescence states, across multiple time points (Fig. 1B; Fig. 2D;
224 Supplemental Data 1). Consistent with decreased accessibility at promoter regions
225 enriched in E2F motifs (Fig. 2B: top; Supplemental Fig. 1C,D), E2F target genes were
226 downregulated in both drug treatments, reflecting the cell cycle arrested state (Fig.
227 2D,E; Supplemental Data 2). We also observed more obvious drug-specific and
228 temporal effects than at the chromatin accessibility and enhancer activation level (Fig.

229 2D). This could be explained by differential transcription factor activity at DNA regulatory
230 elements that are dependent on the DNA damage context. Among the genes that
231 displayed higher expression levels in a drug-specific manner, palbociclib was related to
232 a stronger “Epithelial to Mesenchymal Transition” signature (Fig. 2F; Supplemental Data
233 2). Phosphorylation of p53 at serine 15 has been shown to enhance p53 binding to
234 chromatin, thereby facilitating transcriptional activation at p53-responsive promoters
235 (Loughery et al. 2014). Supporting this notion, doxorubicin preferentially activated the
236 p53 axis, as evidenced by induction of p53 target genes including CDKN1A (encoding
237 p21) (Supplemental Fig. 1H,I), enrichment of the p53 pathway (Fig. 2G; Supplemental
238 Data 2) that was absent in palbociclib, and increased accessibility at p53 motifs
239 (Supplemental Fig. 1G).

240 Further analysis of drug-specific clusters revealed distinct early and late transcriptional
241 responses within each treatment. Notably, while some late-response genes were also
242 upregulated under the alternate condition, their induction was consistently greater in the
243 treatment in which they were classified (Supplemental Fig. 2B: top). The early
244 doxorubicin response was once again centered around p53 (Supplemental Fig. 2B:
245 bottom; Supplemental Data 3), while the later response may involve metabolic
246 adaptation through genes like *PPARGC1A* and *SORL1* (Supplemental Fig. 2B: bottom;
247 Supplemental Data 3).

248 Although there was a large number of transcriptomic changes that were specific to the
249 senescence trigger, we noted a set of genes that increased in expression as cells
250 entered a senescent state independent of treatment (Fig. 2D: Shared-upregulated). This
251 upregulation was faster in the doxorubicin treatment and more gradual with palbociclib,

coinciding with the dynamics of the enhancer activation we noted previously (Fig. 2C). Gene Set Enrichment Analysis (GSEA) revealed this set of genes was enriched for NF-κB transcriptional activity (Fig. 2H; Supplemental Data 2), a motif we also observed among ATAC-seq peaks with shared increased accessibility between treatments (Supplemental Fig. 1E: middle; Supplemental Data 4).

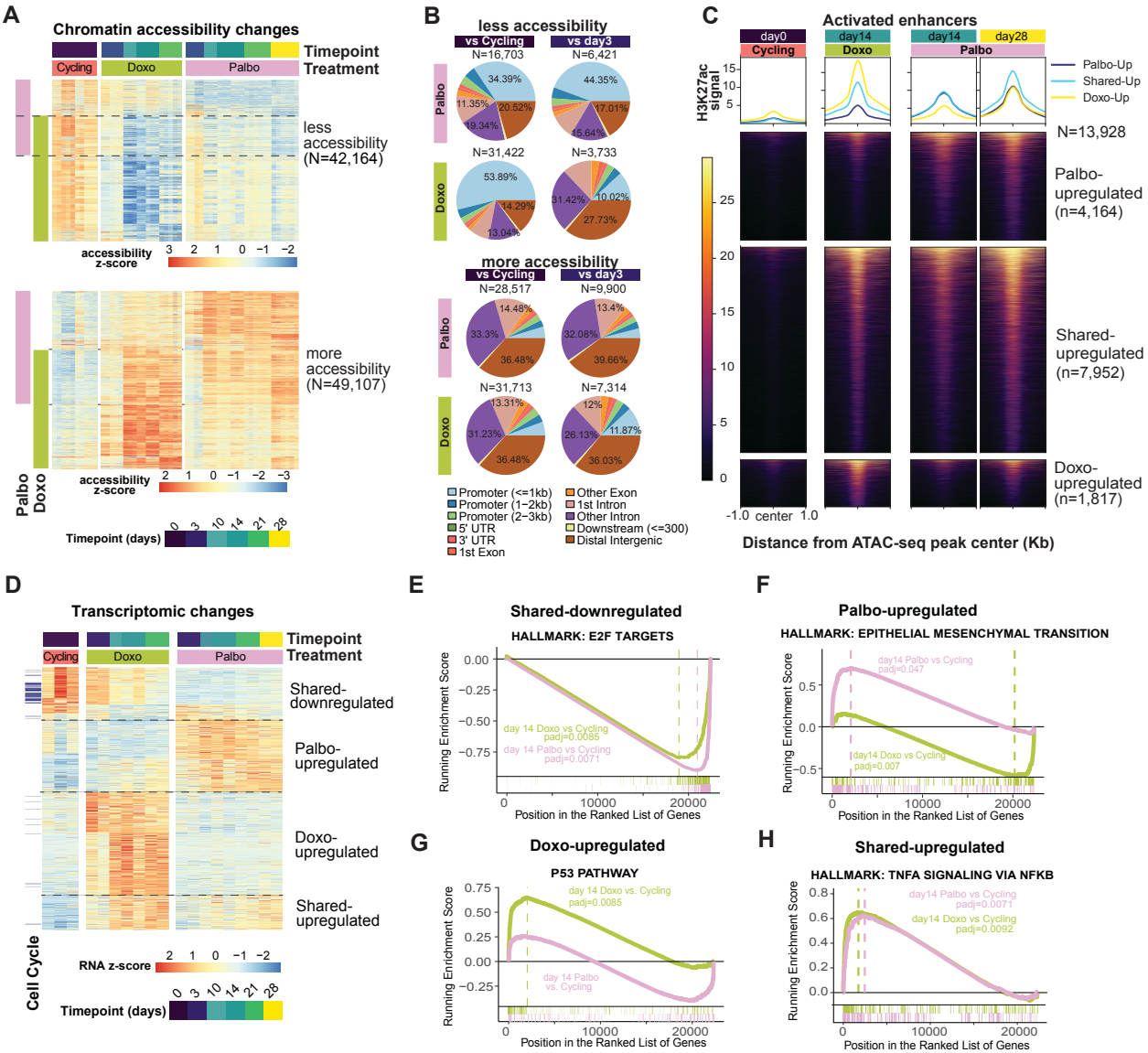

Fig. 2: Distinct and shared transcriptional and chromatin responses define drug-specific senescence trajectories

A. Heatmap of z-scores from VST-normalized read counts under ATAC-seq peaks with significantly less accessibility (top) or more accessibility (bottom) over time, relative to cycling or day 3. Annotations indicate significance in Palbo (pink) or Doxo (green) and their genomic location.
B. Genomic feature annotation of ATAC-seq peaks with less accessibility (top) or more accessibility (bottom), merged across all time points compared to Cycling (left) or day 3 (right)). N= number of peaks in merged peak-set making up the pie chart.
C. RPGC-normalized H3K27ac coverage in drug-activated enhancers (total number N= 13,928). Each row in the heatmap represents a drug-activated enhancer: defined as a region of increased chromatin accessibility overlapping a corresponding H3K27ac region increasing in palbociclib (Palbo-upregulated), both treatments (Shared-upregulated) or doxorubicin (Doxo-upregulated) (See Supplemental Materials). The number of regions plotted is shown on the right. Scale bar represents bigwig signal of normalized coverage.
D. K-means clustered heatmap of z-scores from rlog normalized counts for significantly changing genes across treatment and timepoints (days of treatment). Cell cycle genes annotated in dark green and blue, respectively.
E. GSEA running enrichment score for enriched Hallmark term “E2F TARGETS” identified in Shared-downregulated genes. Ranked gene list is based on day 14 Doxo and day 14 Palbo relative to Cycling comparisons. *Padj* values showing significance of enrichment are shown.
F. GSEA running enrichment score for enriched Hallmark term “EPITHELIAL MESENCHYMAL TRANSITION” identified in Palbo-regulated genes.
G. GSEA running enrichment score for enriched Hallmark term “P53 PATHWAY” identified in Doxo-regulated genes.
H. GSEA running enrichment score for enriched Hallmark term “TNFA SIGNALING VIA NFKB identified in Shared-upregulated genes. *Padj* values showing significance of enrichment are shown.

290 **NF-κB is a predicted transcriptional regulator of the shared SASP in liposarcoma**

291 Although multiple features of therapy-induced senescence vary between doxorubicin
292 and palbociclib treatment responses (e.g., DNA damage activation, p53 signaling, and a
293 large fraction of RNA and chromatin accessibility changes), we were particularly
294 interested in what aspects these two very different drivers of stable arrest have in
295 common. To investigate this, we focused on shared-upregulated genes which had
296 distinct temporal dynamics in expression levels across drug treatments (Fig. 2D), with a
297 strong enrichment in the "TNFA SIGNALING VIA NFKB" Hallmark term (Fig. 2H;
298 Supplemental Data 2).

299 Despite its activity being undetected in prior short-term CDK4/6i treatment studies, the
300 NF-κB complex and its canonical subunit, RELA (p65 or TF65) emerged as top
301 predicted upstream regulators (Fig. 3A; Supplemental Data 2). We identified 40 NF-κB
302 targets within the shared-upregulated gene module and analyzed their RNA levels at
303 days 3 and 14 of treatment (Fig. 3B). Approximately half of these genes were also
304 defined as SASP across multiple databases (Fig. 3B: right; Supplemental Data 1). Both
305 drugs showed a significant increase in expression over time, consistent with a
306 progressive NF-κB response (Fig. 3B). However, this response was delayed in
307 palbociclib-treated cells, with the median fold change at day 14 resembling that of
308 doxorubicin at day 3 (Fig. 3B). Corresponding to the shared induction of NF-κB target
309 genes, NF-κB family motifs were similarly enriched in regions with increased chromatin
310 accessibility in both drugs (Supplemental Fig. 3A; Supplemental Data 4). To confirm this
311 shared NF-κB signature predicted by multi-omics analysis, we performed
312 immunofluorescence on p65 (Fig. 3C; Supplemental Fig. 3B). In both treatments, we

313 observe increased p65 nuclear localization, with timing that correlated approximately
314 with the onset of stable cell cycle arrest (Fig. 1D), i.e., steadily increasing up to day 14
315 in response to palbociclib and much earlier, by day 3, in doxorubicin (Supplemental Fig.
316 3B).

317 **A shared NF-κB-driven SASP program is also found in MCF7 breast cancer cells**

318 A previous study did not report NF-κB activation with 5 days of CDK4/6i treatment using
319 the ER+ breast cancer model cell line, MCF7. Therefore, we wondered whether later
320 timepoints would show NF-κB activation that could regulate the SASP in this system as
321 well. To assess whether delayed NF-κB activation also occurred in this additional
322 clinically relevant model, we treated MCF7 breast cancer cells with 1 μM palbociclib,
323 100 nM doxorubicin, or 100 nM palbociclib and 10 nM fulvestrant (Palbo+Fulv) —the
324 standard of care regimen for ER+ breast cancer.

325 We confirmed that CDK4/6i induces senescence in MCF7 cells without triggering
326 excess DNA damage, beyond what is observed in cycling cells, unlike doxorubicin
327 (Supplemental Fig. 3C-E). We observed increased SA-βgal staining (Supplemental Fig.
328 3C) and reduced clonogenic outgrowth (Supplemental Fig. 3D) across all conditions.
329 While strong stable arrest is observed in Palbo+Fulv, few γH2AX and 53BP1 DNA
330 damage-associated foci accumulated compared to doxorubicin (Supplemental Fig. 3E),
331 consistent with what we see in the liposarcoma context (Fig. 1G,H).

332 Even in a model where NF-κB activity was previously undetected in short-term studies
333 (Lee et al. 2024), we observed the eventual activation of NF-κB as a late treatment
334 response. Time-resolved analysis over the course of 21 days of Palbo+Fulv treatment

335 revealed 7,510 significantly altered genes based on a *Padj* threshold of < 0.05 (Fig. 3D).
336 Strikingly, NF-κB-related pathways were enriched in a group of genes that are modestly
337 upregulated at early time points (days 3-5) but show strong induction after day 10 (Fig.
338 3E, cluster 3). GSEA across different drug conditions in MCF7 samples, showed that
339 the "TNFA SIGNALING VIA NFKB" Hallmark term was significantly enriched in both
340 palbociclib- and doxorubicin-treated samples (Fig. 3F; Supplemental Data 2). Evidence
341 of shared induction of NF-κB activity was further validated by immunofluorescence
342 staining of p65, which showed increased nuclear localization across all drug treatments
343 (Fig. 3G). This supports the notion that NF-κB-SASP network activation is a shared
344 feature of therapy-induced senescence across cancer types.

345 To identify shared NF-κB–associated SASP components, we examined NF-κB target
346 genes upregulated across treatments in MCF7 cells and found that 41 of 116 (35%)
347 were common to palbociclib, Palbo+Fulv, and doxorubicin (Supplemental Fig. 3F). We
348 next assessed conserved SASP programs driven by CDK4/6i across cell types. Several
349 common SASP genes exist, including established NF-κB targets such as CXCL2 and
350 CXCL8, which were consistently upregulated following CDK4/6i treatment in both MCF7
351 and LS8817 cells (Supplemental Fig. 3G). Although not a direct NF-κB target,
352 *ANGPTL4*, a SASP factor necessary for CDK4/6i-mediated stable arrest (Gleason et al.
353 2024), was induced in both cell types. Moreover, *ANGPTL4* activates *IL1A*, a pro-
354 inflammatory cytokine transcribed by NF-κB (Makulyte et al. 2026)—highlighting the
355 complexity of the CDK4/6i-driven SASP, which may include components that can act
356 either upstream or downstream of NF-κB. Together, these findings highlight a shared

357 NF-κB response across distinct senescence-inducing treatments, alongside a CDK4/6i-

358 specific SASP conserved across cancer cell types

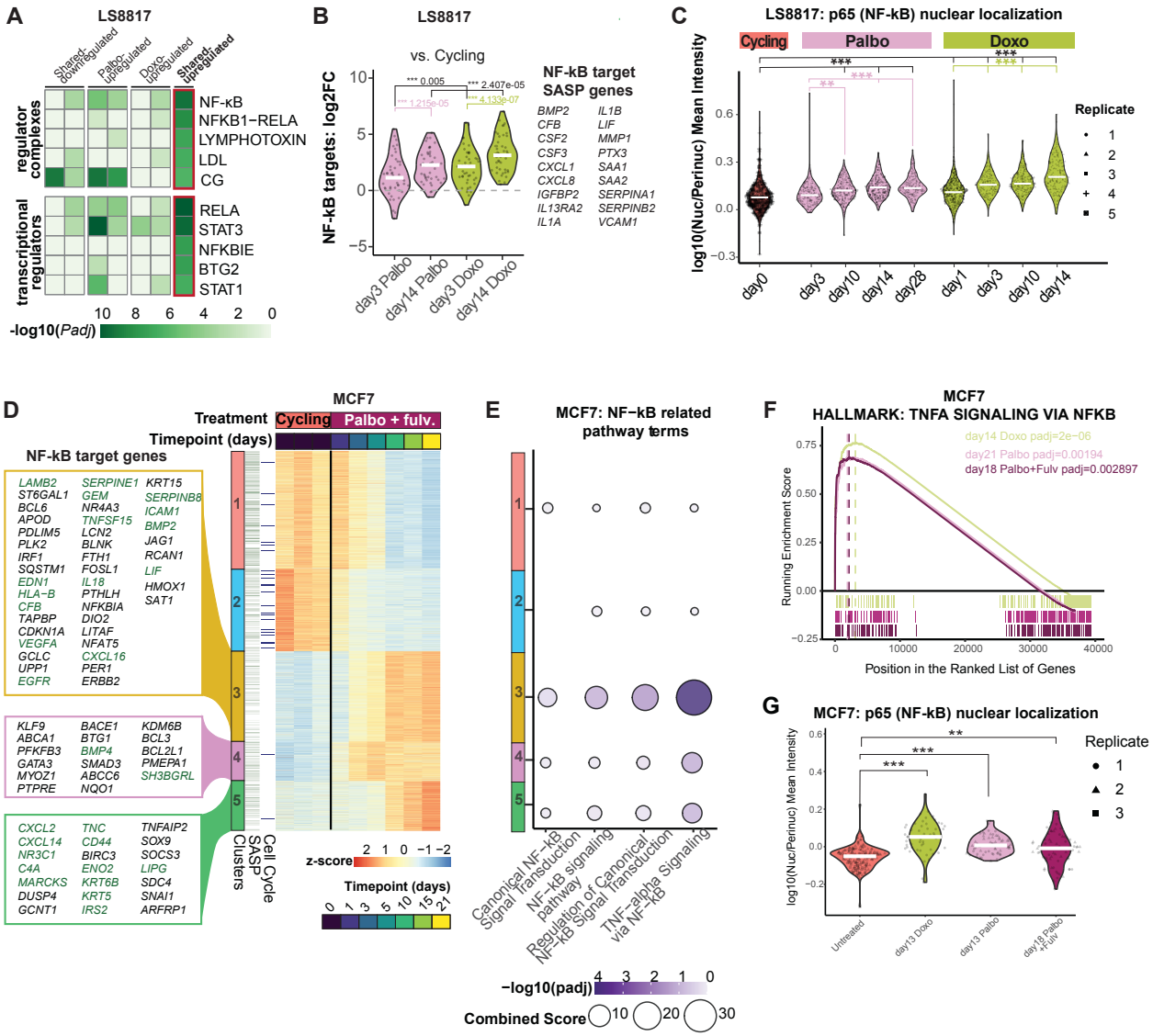

359

Fig. 3: A shared senescence signature driven by NF-κB activation is delayed in CDK4/6i treatment across cancer cell types

A. -Log10(*Padj*) values of top 5 IPA predicted upstream regulator complexes and transcriptional regulators of Shared-upregulated genes relative to other RNA-seq clusters in LS8817 cells.
B. Left: Log2 fold change (log2FC) values of NF-κB target genes that are part of the Shared-upregulated genes (RNA Cluster 7) in day 3 and day 14 Palbo and Doxo relative to Cycling in LS8817 cells. Median log2FC values for each condition are shown as a bold white line. The dotted gray line at log2FC = 0 indicates no change from Cycling. A paired Student's t-test was used to assess significance between log2FC distributions. Right: gene IDs of NF-κB target genes that are also defined as SASP genes based on whether they were classified as such in manually curated databases provided in Wang et al.,(Wang et al. 2022) Gleason et al.,(Gleason et al. 2024) and the SASPAtlas (Basisty et al. 2020).
C. Quantification of log10 ratio of mean intensity of p65 in the nucleus to perinuclear region in LS8817 cells. Statistical significance was calculated using Dunnett's test. Each point is a cell that was quantified.
D. K-means clustered heatmap of z-scores from rlog normalized counts for significantly changing genes across treatment and timepoints (days of treatment) based on RNA-seq performed in MCF-7 cells. SASP and cell cycle genes are annotated in dark green and blue, respectively. NF-kB target genes found in each upregulated gene cluster are shown left of the heatmap. Genes in dark green are also annotated as SASP.
E. GO enrichment results of NF-kB related terms from each RNA-seq cluster in MCF7 cells.
F. GSEA running enrichment score for enriched Hallmark term "TNFA SIGNALING VIA NFKB" for palbociclib, doxorubicin and palbociclib+fulvestrant treatment in MCF7 cells. *Padj* values from GSEA are shown.
G. Quantification of log10 ratio of mean intensity of p65 in the nucleus to perinuclear region in MCF7 cells across different biological replicates. Statistical significance was calculated using Dunnett's test.

391 **Nearby enhancer activation contributes to the induction of shared NF-κB target**
392 **genes**

393 Although NF-κB family motifs were globally enriched in regions of increased
394 accessibility (Supplemental Fig. 3A), we sought to determine whether this enrichment
395 was retained at regulatory elements more likely to directly influence expression levels of
396 shared-upregulated genes. To focus on such elements, we restricted our analysis to
397 nearby upregulated accessible regions, which were defined as within 50kb of genes
398 belonging to the shared-upregulated gene module (Supplemental Data 5). Even under
399 this constraint, we observed that increased Tn5 insertion coverage at TF65 (p65) motifs
400 occurs across both drug treatments (Supplemental Fig. 4A-B).

401 Next, we identified nearby drug-activated enhancers by intersecting upregulated
402 accessible regions with sites of increased H3K27ac, specifically located within 50kb of
403 shared-upregulated genes that increased in expression (Fig. 4A). Notably, H3K27ac
404 accumulation at these nearby enhancers was delayed in CDK4/6i relative to doxorubicin
405 (Fig. 4A: top). Coinciding with the slower kinetics of NF-κB target gene induction in
406 CDK4/6i (Fig. 2D; Fig. 3D), these shared-upregulated enhancers proximal to shared-
407 upregulated genes were highly enriched in NF-κB family motifs, including canonical
408 subunits TF65 and NFKB1 (Fig. 4B: left).

409 In addition, motifs enriched in nearby palbociclib-upregulated enhancers—including
410 CEBPB, GATA3, GATA6, SOX5, and FOXK1 (Fig. 4B: middle)—were also present at
411 nearby shared-upregulated enhancers (Fig. 4B: top), suggesting continual engagement
412 of transcription factors associated with mesenchymal enhancer activity and epithelial-

413 mesenchymal transition programs. In contrast, doxorubicin-upregulated enhancers near
414 shared-upregulated genes were additionally enriched for p53 family motifs (Fig. 4B:
415 right), consistent with activation of the DNA damage response.

416 Interestingly, AP-1 motifs (e.g., FOSB and ATF2), a family of stress-responsive pioneer
417 transcription factors (Biddie et al. 2011; Vierbuchen et al. 2017; Patrick et al. 2024) were
418 also specifically enriched in doxorubicin-responsive enhancers near shared-upregulated
419 genes (Fig. 4B: right). When considering regions gaining accessibility near the same
420 genes, without requiring a change in acetylation, we found that there was some gain of
421 accessibility at AP-1 motifs under palbociclib, but it was more modest than with
422 doxorubicin (Supplemental Fig. 4C, top). Consistently, enrichment of AP-1 motifs in this
423 accessible region set was also present at a low level (Supplemental Fig. 4C, bottom;
424 Supplemental Data 5). However, when considering all upregulated ATAC-seq peaks
425 genome-wide, peaks containing AP-1 motifs were strongly enriched at all times under
426 doxorubicin treatment but also significantly enriched under palbociclib treatment,
427 especially after day 3—exhibiting delayed activation kinetics (Supplemental Fig. 4D;
428 Supplemental Data 4). Given that AP-1 has been identified as a master regulator of
429 oncogene-induced senescence (Martínez-Zamudio et al. 2020), a DNA damage-driven
430 process, the combined enrichment of p53 and AP-1 motifs at doxorubicin-upregulated
431 enhancers may contribute to the earlier and more robust activation of NF-κB compared
432 to CDK4/6i.

433 **Loss of macroH2A is associated with increased expression of NF-κB-driven**
434 **shared SASP genes**

435 In addition to enhancer activation, we wondered if other nearby changes in the
436 epigenome contributed to activation of NF-κB-driven SASP genes. It is thought that the
437 spatial rearrangement of heterochromatin into SAHFs plays a role in silencing cell cycle
438 progression genes (Narita et al. 2003), while allowing for SASP genes to be
439 sequestered into a transcriptionally permissive environment (Aird et al. 2016). Given the
440 role that the histone variant, macroH2A, plays in transcriptional repression and the
441 formation of the SAHFs (Zhang et al. 2005; Zhang et al. 2007), we used CUT&RUN to
442 map the genome-wide distribution of macroH2A1 in late-stage therapy-induced
443 senescence. We find that macroH2A2 is not expressed in this cell line (Supplemental
444 Fig. 4E: top), additionally neither macroH2A1 RNA levels (Supplemental Fig. 4E:
445 bottom) nor its global distribution on chromatin changed with drug treatment
446 (Supplemental Fig. 4F). However, by examining macroH2A1-containing regions found
447 within 50kb of shared-upregulated genes, we observe a striking loss of macroH2A (Fig.
448 4C). Hence, in addition to enhancer activation, locally reduced levels of macroH2A may
449 also contribute to the activation of inflammatory SASP genes, likely through a de-
450 repression mechanism.

451 We also focused on chromatin changes surrounding specific canonical SASP genes
452 upregulated across both treatments. We examined a ~300 kb window around the *IL1A,*
453 *IL1B* (Fig. 4D), *CXCL1*, and *CXCL8* loci (Supplemental Fig. 4G). Across both
454 treatments, we observed shared increases in chromatin accessibility as early as day 3,
455 spanning gene bodies, transcription termination sites, and distal intergenic regions (Fig.
456 4D; Supplemental Fig. 4G). Despite these early accessibility gains, H3K27ac
457 accumulation was delayed, remaining lower at day 14 in CDK4/6i-treated cells

458 compared to doxorubicin before gradually increasing to comparable levels by day 28
459 (Fig. 4D; Supplemental Fig. 4G).

460 Finally, we identified enhancers selectively activated in doxorubicin-treated cells, which
461 may contribute to the earlier and more robust induction of shared SASP genes
462 observed under this condition (Fig. 4D; Supplemental Fig. 4G). Compared to ATAC-seq
463 and H3K27ac signal, macroH2A1 coverage is broader and more diffuse, with signal
464 depletion generally occurring in regions flanking—rather than within—the gene bodies
465 of these inflammatory loci (Fig. 4D; Supplemental Fig. 4G). This pattern is surprising,
466 and suggests an additional regulatory layer beyond the transcribed gene-body
467 macroH2A depletion predicted by the “transcriptional pruning” model (Sun et al. 2018).

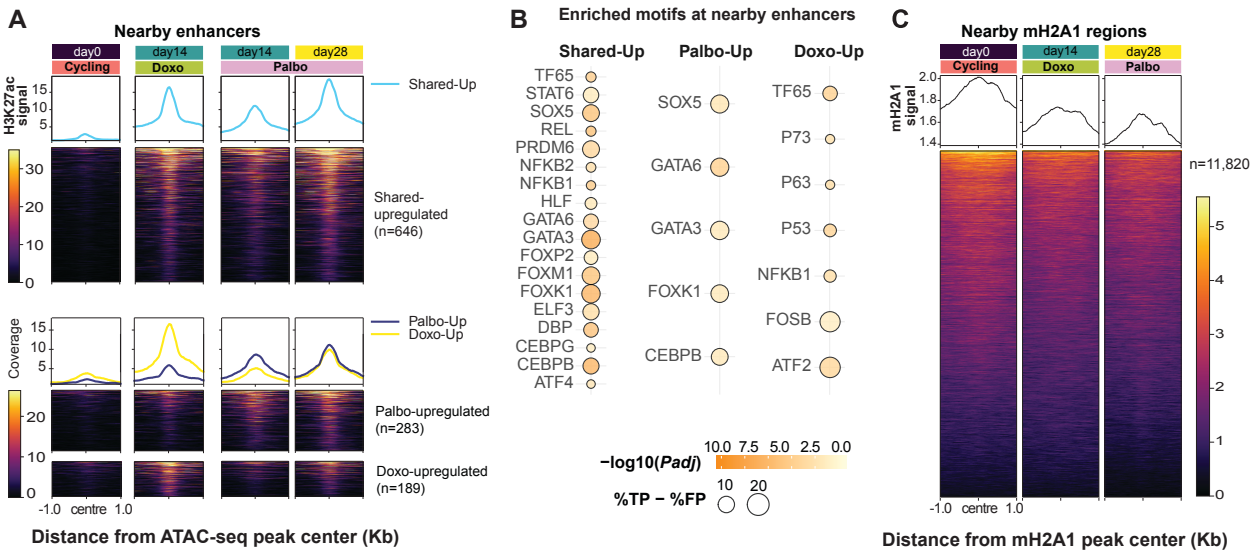
A
Nearby enhancers
day0
Cycling
day14
Doxo
day14
Palbo
day28
H3K27ac signal
Shared-Up
Shared-upregulated (n=646)
Coverage
Palbo-Up
Doxo-Up
Palbo-upregulated (n=283)
Doxo-upregulated (n=189)
-1.0 centre 1.0
Distance from ATAC-seq peak center (Kb)
B
Enriched motifs at nearby enhancers
Shared-Up
Palbo-Up
Doxo-Up
TF65
STAT6
SOX5
REL
PRDM6
NFKB2
NFKB1
HLF
GATA6
GATA3
FOXP2
FOXM1
FOXK1
ELF3
DBP
CEBPG
CEBPB
ATF4
SOX5
GATA6
GATA3
FOXK1
CEBPB
TF65
P73
P63
P53
NFKB1
FOSB
ATF2
−log10(Padj)
10.0 7.5 5.0 2.5 0.0
%TP − %FP
10 20
C
Nearby mH2A1 regions
day0
Cycling
day14
Doxo
day28
Palbo
mH2A1 signal
n=11,820
-1.0 centre 1.0
Distance from mH2A1 peak center (Kb)

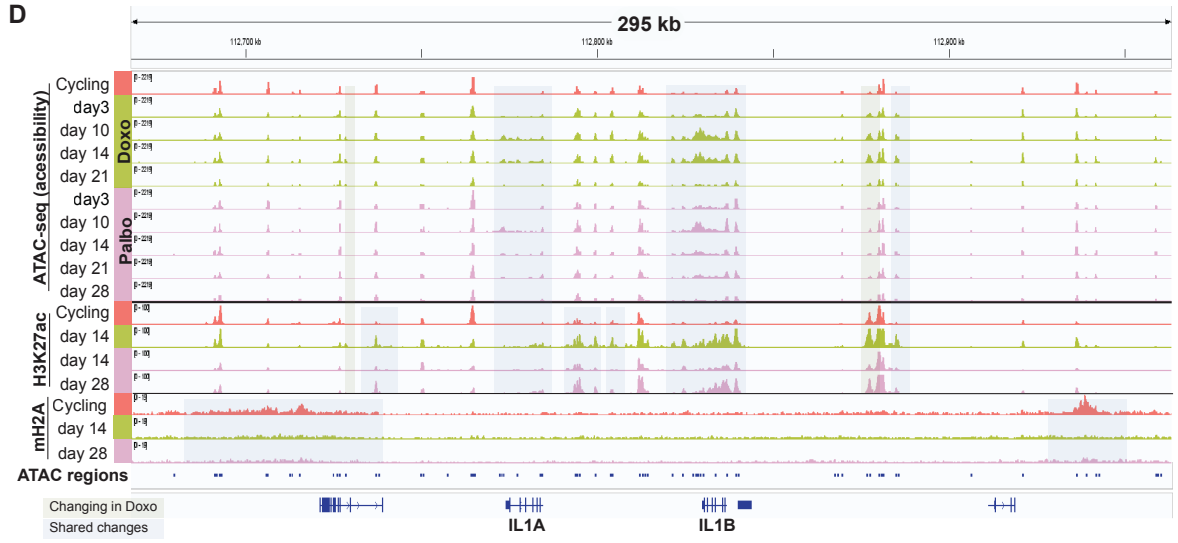
D
295 kb
ATAC-seq (acessibility)
Doxo
Palbo
Cycling
day3
day 10
day 14
day 21
day3
day 10
day 14
day 21
day 28
H3K27ac
Cycling
day 14
day 14
day 28
mH2A
Cycling
day 14
day 28
ATAC regions
Changing in Doxo
Shared changes
IL1A
IL1B

468

Fig. 4: Activation and loss of macroH2A at enhancers near NF-κB-driven shared SASP genes

A. H3K27ac coverage signal across conditions in drug-activated enhancers within 50kb of shared-upregulated genes (Nearby enhancers). Each row in the heatmap represents a drug-activated enhancer: defined as a region of increased chromatin accessibility overlapping a corresponding H3K27ac region increasing in palbociclib (Palbo-upregulated), both treatments (Shared-upregulated) or doxorubicin (Doxo-upregulated) (See Supplemental Materials). The number of nearby peaks is shown on the left. Scale bar represents bigwig signal of normalized coverage.
B. Motif enrichment results of drug activated enhancers shown in (A) within 50kb of Shared-upregulated genes. Dot intensity represents -log10(p-adj) values, while dot size reflects the difference between true positive and false positive peaks (%TP - %FP).
C. macroH2A1 (mH2A1) signal for all mH2A1 peaks within 50kb of shared-upregulated genes (nearby mH2A1 regions) from Fig. 2D. The number of nearby mH2A1 peaks is shown on the left. Scale bar represents bigwig signal of normalized coverage.
D. Genome browser view of *IL1A* and *IL1B* loci. Normalized bigwig tracks for ATAC-seq, H3K27ac and macroH2A1 (mH2A) are shown. Upregulated regions occurring in both treatments are highlighted in blue (Shared changes) while Doxo-upregulated regions are highlighted in green (Changes in Doxo).

489 **The NF-κB-driven shared SASP component can be uncoupled from stable cell**
490 **cycle arrest**

491 We next considered whether NF-κB activation was necessary for cells to drive stable
492 arrest, or is it solely responsible for the shared SASP program without any additional
493 effects on senescence? We attempted to alter the NF-κB-driven shared SASP response
494 through pharmacological inhibition with BAY11-7082 (BAY) (Pierce et al. 1997) during
495 both treatments, after senescence was established (Fig. 5A). Principal component
496 analysis shows NF-κB inhibition had minimal impact on the overall transcriptome, as
497 BAY- and DMSO-treated samples clustered together within each drug group (Fig. 5B).
498 However, BAY suppressed expression of key shared NF-κB target SASP genes,
499 *CXCL1, CXCL8, IL1A, IL1B, GMCSF* (*CSF2*), *IL6* and *SOD2* (Fig. 5C; Supplemental
500 Fig. 5A,B).

501 Beyond these, NF-κB inhibition downregulated 57 shared genes, as well as additional
502 drug-specific targets (Supplemental Fig. 5C), suggesting that while NF-κB is a common
503 feature of senescence, its ability to regulate specific targets may differ across
504 treatments. Like previous studies of NF-κB in other types of senescence (Chien et al.
505 2011a; Lau and David 2019), inhibiting its activity was not enough to reverse
506 senescence, as indicated by no differences in clonogenic outgrowth assays (Fig. 5D).
507 Hence, although NF-κB activation does not appear to be necessary for maintaining
508 stable arrest, it is responsible for driving part of the inflammatory SASP response.

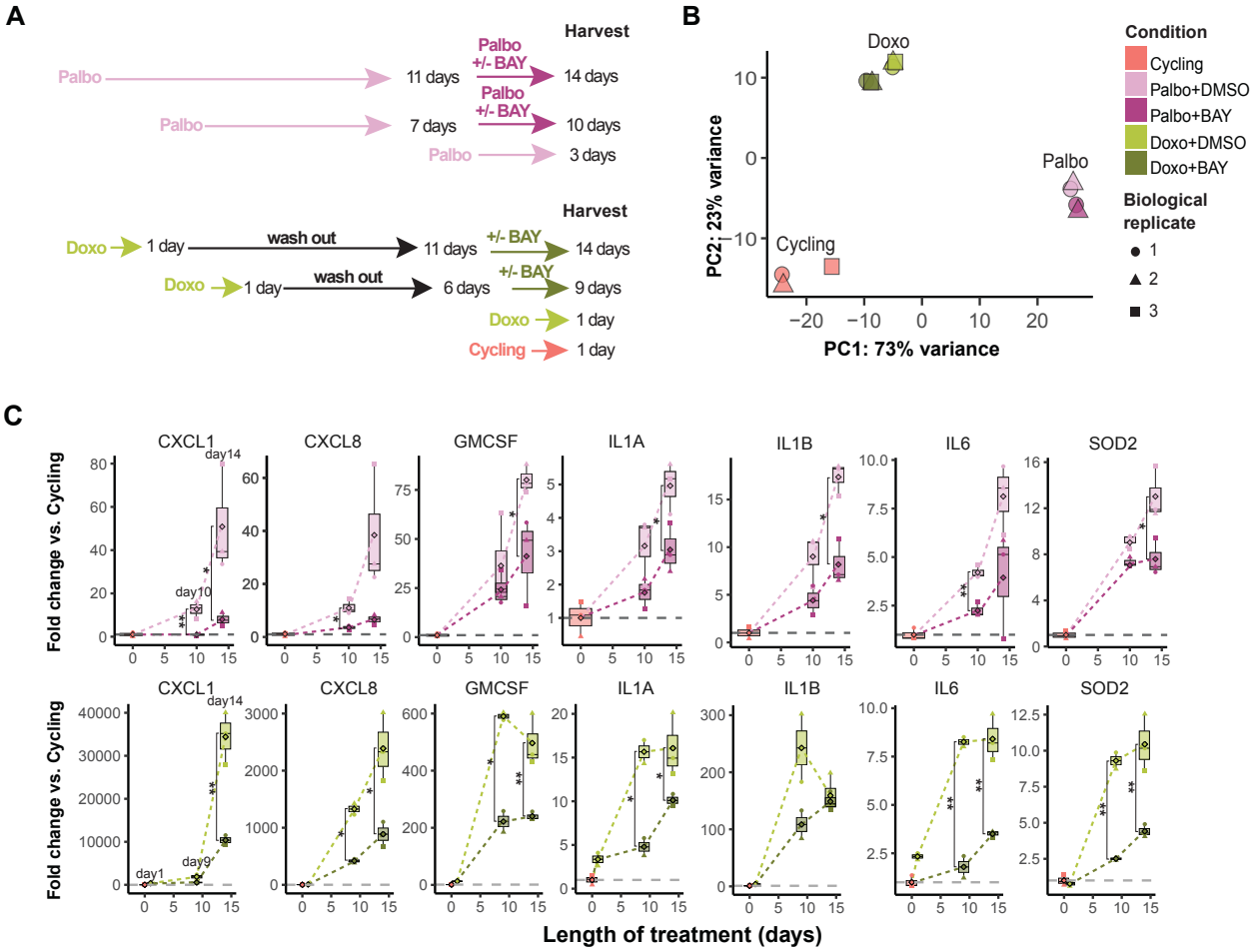
A
Harvest
Palbo
11 days
Palbo +/- BAY
14 days
Palbo
7 days
Palbo +/- BAY
10 days
Palbo
3 days
Harvest
Doxo
1 day
wash out
11 days
+/- BAY
14 days
Doxo
1 day
wash out
6 days
+/- BAY
9 days
Doxo
1 day
Cycling
1 day
B
Doxo
Palbo
Cycling
PC2: 23% variance
PC1: 73% variance
Condition
Cycling
Palbo+DMSO
Palbo+BAY
Doxo+DMSO
Doxo+BAY
Biological replicate
1
2
3
C
CXCL1
CXCL8
GMCSF
IL1A
IL1B
IL6
SOD2
Fold change vs. Cycling
day1
day9
day10
day14
Length of treatment (days)

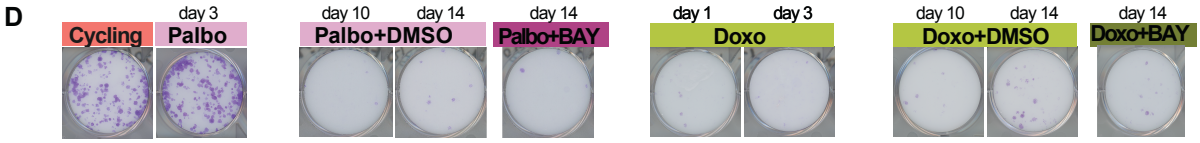
D
Cycling
day 3
Palbo
day 10
day 14
Palbo+DMSO
day 14
Palbo+BAY
day 1
day 3
Doxo
day 10
day 14
Doxo+DMSO
day 14
Doxo+BAY

509

510 **Fig. 5: Inhibition of NF-kB activity suppresses the shared SASP without reversing**
511 **stable growth arrest**

512 A. Schematic of pharmacological inhibition of NF-κB with BAY11-7082 (BAY) in LS8817
513 cells (see Methods). 10 μM BAY or equivalent volume of DMSO (negative control)
514 was added to cells for 2-3 days prior to harvest.
515 B. Principal component analysis on RNA-seq of day14 palbociclib or doxorubicin
516 treated LS8817 cells with or without NF-κB inhibitor, BAY11-7082 (BAY).
517 C. RT-qPCR results of palbociclib or doxorubicin treated LS8817 cells with or without
518 BAY. Relative fold change values to Cycling are shown. Dotted grey line indicates no
519 change. Diamonds inside boxplot represent the mean fold change value. Circles,
520 triangles, and rectangles represent the fold change of individual biological replicate.
521 Dark purple and dark green shades indicate Palbo and Doxo samples treated with
522 BAY while lighter purple and green shades indicate samples that had DMSO added
523 at the same time as BAY samples. Statistical significance was calculated using a
524 two-tailed t-test.
525 D. Crystal violet staining after clonogenic outgrowth after palbociclib or doxorubicin
526 treatment +/- BAY. 800 cells were seeded per well in a 6-well plate and grown in
527 drug-free media for 12 days after harvest.
528

529 **DNA damage response pathway is upstream of NF-κB nuclear localization in**
530 **doxorubicin but not CDK4/6i**

531 NF-κB activity can be triggered by a variety of cellular stressors, among which the DNA
532 damage response (DDR) is a major contributor (Miyamoto 2011). Notably, several
533 contexts, such as mitochondrial dysfunction and treatment with histone deacetylase
534 inhibitors, have demonstrated that senescence-associated DDR signaling can be
535 engaged in the absence of overt DNA damage (Pospelova et al. 2009; Pazolli et al.
536 2012; Wiley et al. 2016).

537 While CDK4/6 inhibition does not directly induce DNA damage, these previous studies
538 raise the possibility that DDR components could nonetheless be engaged through other
539 mechanisms. To test whether DDR signaling contributes to NF-κB activation in this
540 context, we pharmacologically inhibited the key DDR kinases ATM and ATR in arrested
541 LS8817 cells (Supplemental Fig. 6A). We confirmed that the DDR signaling was
542 dampened by ATM and ATR inhibition by immunoblotting for phosphorylated (phospho-)
543 p53 (Fig. 6A; Supplemental Fig. 6B) and Chk2 (Fig. 6C; Supplemental Fig. 6C).
544 Phospho-p53 is largely absent following palbociclib treatment, and co-treatment with
545 ATM and ATR inhibitors did not alter phospho-p53 levels (Fig. 6A). Phospho-Chk2 levels
546 were modestly increased under palbociclib treatment, suggesting mild ATM activation in
547 the absence of p53 activation and additional DNA damage (Fig. 6B). In contrast,
548 doxorubicin treatment induced robust p53 and Chk2 phosphorylation and activation,
549 which was attenuated by ATM and ATR inhibition (Fig. 6A,B). This corresponded with
550 reduced p65 nuclear localization, consistent with DNA damage-dependent activation of
551 NF-κB (Fig. 6C). In contrast, inhibiting ATM and ATR did not affect NF-κB nuclear

552 localization in CDK4/6i-treated cells (Fig. 6C), indicating that NF-κB activation in this
553 setting occurs independently of the canonical DDR pathway.

554 **ECM driven SASP is specifically activated in CDK4/6i-induced senescence**

555 Given that inhibition of DNA damage response factors did not affect NF-κB nuclear
556 localization in CDK4/6i-treated cells, we next sought to identify alternative upstream
557 pathways by characterizing gene expression programs specific to CDK4/6i-induced cell
558 cycle arrest. Notably, genes associated with TGF-β signaling, including ligands
559 (Supplemental Fig. 6D) and receptors (Supplemental Fig. 6E), were selectively
560 upregulated in CDK4/6i-treated cells, but not in doxorubicin-treated cells. In addition,
561 many of these genes encode ECM components and established TGF-β targets, several
562 of which have been identified as SASP genes in other contexts (Fig. 6D). These findings
563 suggest that, in parallel to the later NF-κB-driven shared SASP, CDK4/6 inhibition
564 promotes an earlier, ECM-enriched SASP program.

565 Consistent with a role for extracellular signaling in this context, *IL1R1*, the primary
566 receptor that *IL1A* and *IL1B* binds to (Wesche et al. 1997), increases in expression
567 during CDK4/6i treatment (Supplemental Fig. 6F: top). This indicates potential activation
568 of cell surface receptors that could drive downstream NF-κB activation. We also
569 detected increased expression of TLR4 in both treatment conditions (Supplemental Fig.
570 6F: bottom), pointing to pattern recognition receptor signaling as an additional route to
571 NF-κB activation (Kelsh and McKeown-Longo 2013; Guo et al. 2024). We hypothesize
572 that upregulation of multiple cell surface receptors—including *TGFBR1/2, IL1R1*, and
573 *TLR4* (Supplemental Fig. 6D-F)—along with ECM-enriched SASP components (Fig. 6D)

574 that engage these receptors, may provide alternative routes to NF-κB activation in

575 CDK4/6i-induced senescence, independent of intrinsic DNA damage signaling (Fig. 6E).

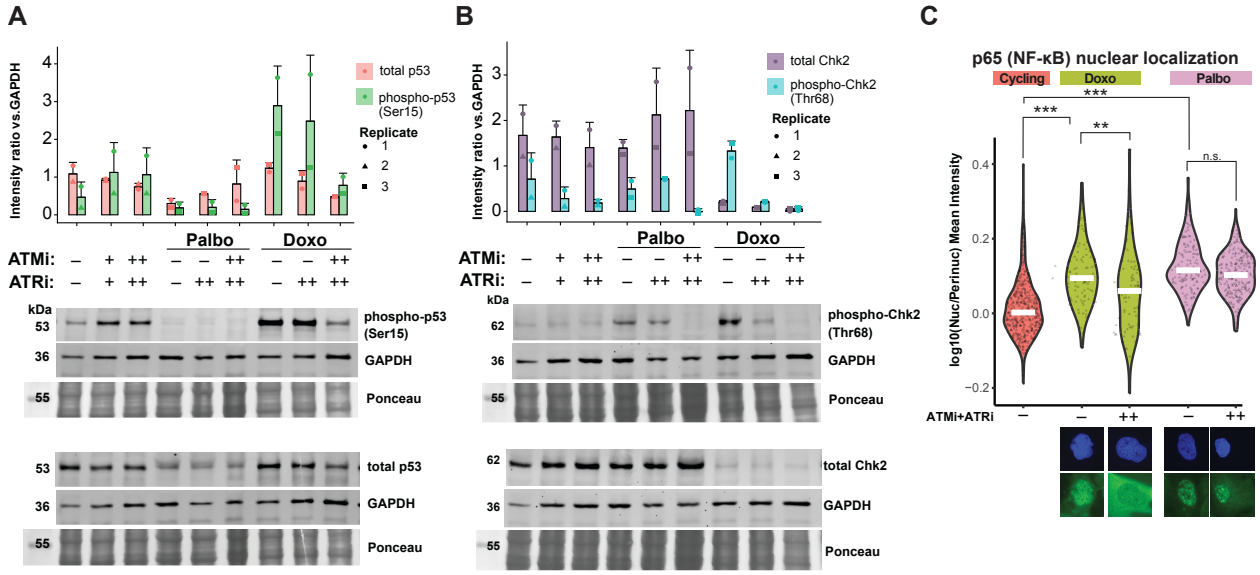

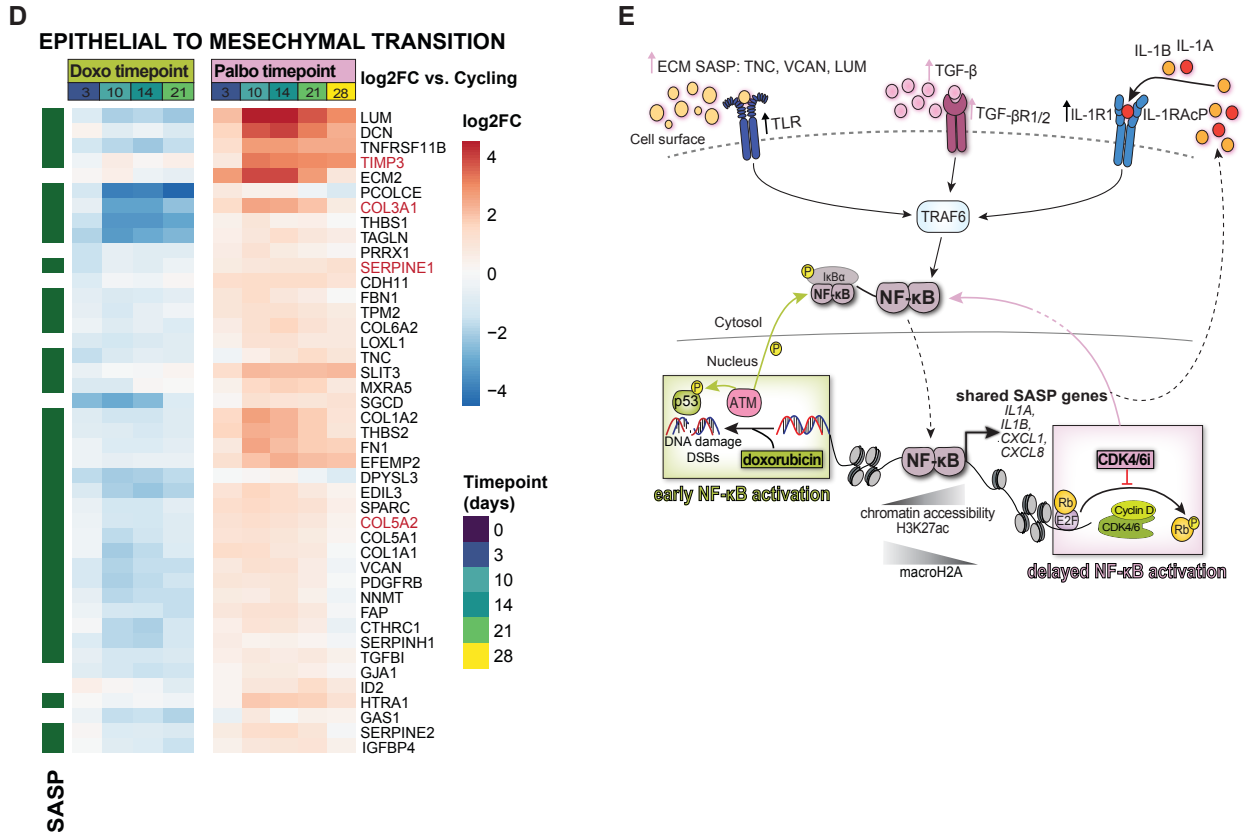

576

577 **Fig. 6: Inhibiting ATM and ATR affects NF-κB nuclear localization in doxorubicin**
578 **but not CDK4/6i therapy-induced senescence**

579 A. Western blots of LS8817 cells treated with Palbo (17 days) or Doxo (7 days), with or
580 without ATR inhibition (ATRi; 4 μM AZD6783) or combined ATR and ATM inhibition
581 (ATRi + ATMi: 4 μM AZD6783 + 4 μM KU-60019) for two biological replicates
582 (Bioreps). ATR and ATM inhibitors were added after cell-cycle arrest had been
583 established. ImageJ quantification of signal relative to GADPH loading control
584 (Top). Phospho-p53 (Ser15) relative to total p53 (Bottom). "–" indicates DMSO
585 control; "+" and "++" indicate 2 μM and 4 μM inhibitor, respectively. Replicate
586 indicates different biological replicates.
587 B. Same as (A) but western blots for phospho-Chk2 (Thr68) relative to total Chk2.
588 C. Quantification of log10 ratio of mean intensity of p65 in the nucleus to perinuclear
589 region in LS8817 cells treated with ATMi+ATRi or DMSO. Statistical significance
590 was calculated using Dunnett's test. Representative images taken at 60x objective
591 magnification of different amounts of p65 nuclear localizations in each condition are
592 shown at the bottom.
593 D. Log2 fold change (log2FC) values of Palbo-upregulated genes that are under the
594 Hallmark term "EPITHELIAL TO MESENCHYMAL TRANSITION", across different
595 timepoints (days of treatment) and drug conditions, relative to Cycling or day 3
596 controls for each drug treatment. Genes that are also SASP are shown on the left in
597 dark green. Genes that are also NF-κB targets are shown in red text.
598 E. Summary model showing possible pathways activated by CDK4/6i and doxorubicin
599 to induce the shared SASP driven by NF-κB at different temporal rates.

600 **DISCUSSION**

601 Therapeutic response in various cancers is in part determined by how effectively tumors
602 are driven into stable growth arrest. However, even upon entering such a senescent
603 state, the profile of secreted molecules, or SASP, plays an important role in influencing
604 the neighboring environment (Wang et al. 2024). Unlike replicative senescence that
605 arises over a lifetime (McHugh and Gil 2018), therapy-induced senescence-like states
606 are acute responses to cancer treatments, exhibiting many features of canonical
607 senescence although mediated through distinct mechanistic triggers (Wagner and Gil
608 2020; Wang et al. 2020; Schmitt et al. 2022). Such acute models of senescence offer
609 new insights into the underlying networks that are accessed during these processes and
610 assist us in revealing common underlying features of the elusive core components of
611 what it means to be a senescent cell. Additionally, understanding how the composition
612 of the SASP changes over time across different cancer therapies will be essential in
613 identifying new targeted approaches that improve patient outcomes.

614 Here we have used a dedifferentiated liposarcoma patient-derived cell line known to
615 enter senescent-like states in response to CDK4/6i, and identified NF-κB as a key
616 regulator of the common SASP inflammatory response. We show that this module of the
617 response arises despite being triggered by a DNA-damaging agent (i.e., doxorubicin) or
618 a DNA damage-independent mechanism (i.e., the CDK4/6 inhibitor palbociclib), and can
619 be decoupled from stable arrest. We confirm this shared NF-κB activation also occurs in
620 an estrogen receptor-positive (ER+) breast cancer cell line model (MCF7), supporting
621 the generality of this regulatory node as a key feature of therapy-induced SASP. While
622 the use of cell line models does not allow for the assessment of the SASP's effects on

623 immune clearance and/or evasion, we sought to focus on the molecular landscape of
624 the tumor cell to clarify this context. Therefore, we mapped the temporal dynamics of
625 epigenomic and transcriptomic networks at different phases of the CDK4/6i-induced
626 senescence, by analyzing the genome-wide chromatin accessibility, H3K27ac-marked
627 enhancers, and mRNA levels at early quiescent (day 3), mid transition (day 14), and late
628 senescent (day 28) timepoints (Fig. 1B). We compared this to the DNA damage-induced
629 senescent state that arises rapidly upon doxorubicin exposure.

630 Most transcriptomic changes are drug-distinct differences explained by p53 activation
631 specific to DNA damage induced by doxorubicin (Fig. 2D,G) and a CDK4/6i-specific
632 treatment response characterized by increased expression of ECM-related genes (Fig.
633 2D,F; Supplemental Fig. 2B). Nonetheless, we identified a common SASP-associated
634 enhancer module enriched for NF-κB motifs that displayed delayed activation in
635 CDK4/6i relative to doxorubicin, which was further substantiated by later accumulation
636 of H3K27ac at enhancer elements (Figs. 2B,3A-B,4A-B). A concurrent loss of the SAHF
637 component macroH2A around these loci may further contribute to the induction of the
638 shared SASP module (Fig. 4C). While loss of macroH2A has been linked to de-
639 repression of inflammatory loci in oncogene-induced senescence (Chen et al. 2015), to
640 our knowledge this is the first report of its depletion in CDK4/6i-induced senescence,
641 although its functional role here remains to be determined.

642 Our data reveal a previously underappreciated inflammatory component of CDK4/6i-
643 induced senescence, with potential implications for long-term therapeutic outcomes.
644 Although NF-κB's role in senescence induced by oncogene activation is established
645 (Chien et al. 2011a; Salminen et al. 2012), its activation in CDK4/6i-induced senescence

646 was surprising, as prior studies failed to detect NF-κB activity (Goel et al. 2017; Wang et
647 al. 2022; Lee et al. 2024). This discrepancy likely reflects differences in the duration of
648 treatment, as these studies were focused on early responses. We did not detect NF-κB
649 activation in earlier timepoints, in line with a previous observation in MCF7 cells after
650 five days of treatment (Lee et al. 2024). However, by increasing the duration of CDK4/6i
651 treatment (i.e., 14, 21, 28 days) we observed delayed but robust NF-κB activation
652 across both liposarcoma and breast cancer cells.

653 To determine whether the NF-κB-driven inflammatory response is necessary for the cell
654 to enter stable arrest, we showed that important shared SASP factors *(CXCL1, CXCL8*,
655 *IL6*, *IL1A*, and *IL1B*) can be effectively suppressed by NF-κB inhibition *without reversing*
656 *stable arrest* (Fig. 5 A-D). Many of these shared SASP factors have known tumor-
657 promoting functions, including immunosuppression, metastasis, and chemoresistance
658 (Ancrile et al. 2007; Acosta and Gil 2009; Jones and Jenkins 2018; Lau and David 2019;
659 Rebe and Ghiringhelli 2020; Garlanda and Mantovani 2021; Wu et al. 2022). The SASP
660 may therefore be tunable by adjuvant therapies to diminish pro-tumorigenic side effects.

661 Beyond shared targets, CDK4/6i also induces a distinct ECM-enriched SASP program
662 (Fig. 6D) that may be driven by TGF-β signaling (Supplemental Fig. 2B,6D-E) and its
663 downstream transcription factors (Fig. 4B). Future work is needed to understand the
664 interplay and regulation between CDK4/6i-distinct and shared components of the SASP.
665 Nonetheless, our data support a growing shift in the way we think about the clinical
666 implications of CDK4/6i treatment. While it may offer initial benefits to patients over
667 traditional chemotherapy, over time it leads to the emergence of a pro-inflammatory

668 SASP driven by NF-κB that can promote tumor progression. Further therapeutic options
669 that modulate the SASP while maintaining arrest are an area ripe for development.

670 These findings improve our understanding of the questions we set out to answer
671 regarding the dependence of the SASP on DNA damage and the dynamic nature of the
672 epigenetic changes that underlie the response. Since macro was previously shown to
673 activate enhancers in response to CDK4/6i in breast cancer (Watt et al. 2021), we
674 asked whether increased accessibility at AP-1 motifs contributed to the differences in
675 the temporal activation of the SASP. In our data, both drug treatments showed evidence
676 of AP-1 activation but exhibited distinct kinetics: rapidly increased in doxorubicin and
677 more gradual with CDK4/6i (Supplemental Fig. 4C-D), with additional AP-1 enrichment
678 at Doxo-specific increased H3K27ac regions. This may indicate that doxorubicin triggers
679 full enhancer activation at AP-1 bound sites, whereas palbociclib treatment merely
680 causes AP-1 factors to open chromatin via pioneering activity (Biddie et al. 2011;
681 Vierbuchen et al. 2017). AP-1 is known to act synergistically with NF-κB to drive the
682 expression of its target genes through genome-wide chromatin remodeling (Fujioka et
683 al. 2004; Oeckinghaus et al. 2011; Ji et al. 2019), which offers an explanation for the
684 timing and magnitude differences of NF-κB-driven SASP activation across treatments;
685 earlier and robust in doxorubicin but delayed in CDK4/6i.

686 An outstanding question is, what drives NF-κB activation in CDK4/6i-induced
687 senescence in the absence of DNA damage? Inhibition of ATM and ATR does not affect
688 NF-κB nuclear localization with CDK4/6i but indeed blocks this response with
689 doxorubicin (Fig. 6C), supporting a DNA damage response-independent mechanism in
690 the CDK4/6i context. Therefore, NF-κB activation in CDK4/6i treatment is likely

691 mediated through alternative upstream pathways, which we suspect includes TGF-β
692 and IL-1, known mediators of this pathway (Guo et al. 2024). Both *TGFBR1/2* and
693 *IL1R1* expression levels are upregulated in CDK4/6i treatment (Supplemental Fig. 6D-
694 F), and converge on the TRAF6-TAK1 signaling axis, resulting in nuclear localization of
695 NF-κB (Freudlsperger et al. 2013; Wang et al. 2021). In addition, both CDK4/6i and
696 doxorubicin treatment cause increased expression of *TLR4*, another cell surface
697 receptor that feeds into NF-κB activation (Guo et al. 2024). *TLR4* can be activated by
698 endogenous damage-associated molecular patterns (DAMPs), including ECM
699 components, versican (*VCAN*) and tenascin C (*TNC*) (Kelsh and McKeown-Longo
700 2013; Han et al. 2020), which are part of the CDK4/6i-enriched SASP (Fig. 6E).
701 Activation of NF-κB promotes continued upregulation of *IL1A* and *IL1B* (Figs. 3B,4D),
702 resulting in a positive feedback loop that sustains NF-κB activity (Croston et al. 1995;
703 Weber et al. 2010). Together, our data suggest a model to be tested in future studies
704 (Fig. 6E), whereby NF-κB activation in CDK4/6i-treated cells arises gradually through
705 upregulation of cell-surface receptors and extracellular signaling rather than acute DNA
706 damage.

707 Our results underscore two important considerations: (1) the importance of the
708 underlying chromatin landscape that can vary intrinsically by cell type and extrinsically
709 by trigger response, and (2) the dynamic and tunable nature of the SASP. In conclusion,
710 we propose a model in which both doxorubicin and CDK4/6i induce senescence through
711 distinct molecular mechanisms that converge over time, leading to NF-κB activation
712 through enhancer remodeling and loss of macroH2A. These epigenetic changes
713 promote a shared senescence response that manifests as a common set of cytokines

714 and chemokines, which are secreted as part of the SASP. Our results bring new insights
715 that help explain conflicting reports on various features of therapy-induced senescence,
716 including the involvement of NF-κB in therapeutics that act via a DNA damage-
717 independent mechanism.

718 **MATERIALS AND METHODS:**

719 **Cell lines and cell culture**

720 Human LS8817$^{\text{TetON FLAG-MDM2}}$ liposarcoma cell line was a gift from Dr. Andrew Koff's
721 laboratory at Memorial Sloan Kettering Cancer Center and has been extensively
722 characterized in the literature (Singer et al. 2007; Barretina et al. 2010; Brill et al. 2010;
723 Gobble et al. 2011; Miller et al. 2013; Kovatcheva et al. 2015). LS8817 have previously
724 been described using the nomenclature DDLS8817 (RRID:CVCL_M814). Cells were
725 cultured in DMEM high glucose no glutamine (Cat# 11960044, Gibco), supplemented
726 with 9% Fetal Bovine Serum (Cat# 10082147, Gibco™), 1% of 100x GlutaMAX™
727 Supplement (Cat# 35050061, Gibco™) and 1% of 10,000U/mL Penicillin/Streptomycin
728 (Cat# 15140122, Gibco™) and maintained at 37°C and 5% CO_2. Cells were
729 authenticated by performing STR profiling to another LS8817 isogenic cell line. Cells
730 were passaged at a 1:3 ratio every 3 days and regularly tested for mycoplasma.

731 Human MCF-7 cells (RRID:CVCL_0031) were cultured in in 75 cm2 flasks DMEM/F-12
732 (#Cat 10565018, Thermo Fisher Scientific) supplemented with GlutaMAX, 10% Fetal
733 Bovine Serum (Cat# F4135, Sigma-Aldrich) and 1% Penicillin-Streptomycin at 37 °C
734 and 5% CO_2. Prior to their use, MCF7 cell identity was verified by STR profiling.

735 **Drug treatments**

736 Cells were passaged at a 1:3 ratio one day before drug treatment. For samples sent for
737 sequencing, cells were treated with either 1 μM palbociclib (Cat# S1116, Selleck
738 Chemicals) or 100 nM doxorubicin (Cat# S1208, Selleck Chemicals), with media changes
739 every 2–3 days until harvest.

740 For NF-κB inhibition experiments, 10 μM BAY11-7082 (Cat# S2913, Selleck Chemicals)
741 was co-administered with 1 μM palbociclib in cells that had been treated with palbociclib
742 3 days before harvest. For the corresponding timepoints in Doxo, cells were treated with
743 100 nM doxorubicin for 24 hours, after which the drug was washed out. 10 μM BAY11-
744 7082 was then added for 2–3 days prior to harvesting the Doxo-treated cells.

745 For ATMi + ATRi experiments, LS8817 cells were first treated for 3 days with 1 μM
746 palbociclib and 100 nM doxorubicin. At day 3, cells treated with palbociclib continued to
747 receive palbociclib with the addition of ATRi (AZD6783 at 4 μM; Cat #T3338, TargetMol),
748 ATMi + ATRi (4 μM KU-60019; Cat #S1570, SelleckChem + 4 μM AZD6783) or equal
749 volume of DMSO as vehicle control. Doxorubicin was washed out after ~3 days before
750 addition of DMSO, ATMi, ATRi or ATMi+ATRi treatment until harvest. Fresh drug-
751 containing media was changed every 2-3 days until harvest.

752 Stock solutions were prepared as followed: palbociclib (10 mM in ultrapure dH_2O, stored
753 at -80°C), doxorubicin (1 mM in ultrapure dH_2O, stored at -20°C), BAY11-7082 (50 mM in
754 DMSO, stored at -80°C), KU-60019 (10 mM in DMSO, , stored at -80°C), AZD6783 (10
755 mM in DMSO, stored at -80°C)

756 **Immunofluorescence**

757 50,000-60,000 cells were plated on acid washed glass coverslips and allowed to adhere
758 overnight. Cells were fixed for 15 minutes with 4% formaldehyde followed by
759 permeabilization with 0.1% Triton-X. Blocking was done with 0.5% Tween-20 and 1%
760 normal goat serum for 30 minutes-1 hour at room temperature (RT).

761 Antibody dilutions used: ATRX (Cat# A301-045A, Bethyl) 1:2000, macroH2A (Cat# sc-
762 377452, Santa Cruz) 1:500, γH2A.X (Cat# 05-636, Millipore) 1:1000, 53BP1 (Cat#
763 ab172580, Abcam) 1:1000, NF-κB p65 (Cat #8242, Cell Signaling Technology) 1:800.

764 Primary antibody incubations were done at 4°C overnight. The next day, secondary Alexa
765 Fluor™ antibodies (Cat #A-11004, A-11008, Invitrogen) were diluted 1:500 with 1:2000
766 Hoechst (Cat #H3570, Fisher Scientific) and incubated for 1 hour at RT. All reagents,
767 including antibodies, were diluted in 1X PBS. All steps were followed by 3 washes of 1X
768 PBS. Coverslips were mounted on homemade mounting medium (1 mL 10X PBS, 9 mL
769 Ultrapure glycerol and 50mg of N-propyl gallate (Cat# A10877-06, Alfa Aesar)).

770 All images were acquired using the Nikon Ti2E Research Microscope System where
771 about 100 nuclei or more were used for downstream quantification. To quantify ATRX,
772 macroH2A, γH2AX, and 53BP1 foci in immunofluorescent images, we used a custom
773 CellProfiler pipeline (Stirling et al. 2021). Foci and nuclei were identified using the
774 **IdentifyPrimaryObjects** module, with the **EnhanceOrSuppressFeatures** module
775 applied beforehand to improve foci detection. The **RelateObjects** module was then used
776 to associate foci with their respective nuclei.

777 The NF-κB nuclear-to-perinuclear intensity ratio was calculated using a CellProfiler
778 pipeline based on https://www.youtube.com/watch?v=DlQSgDlGuds. Briefly,
779 **IdentifyPrimaryObjects** detected nuclei, followed by **ExpandOrShrinkObjects** to
780 expand nuclear boundaries, and **IdentifyTertiaryObjects** to define the perinuclear region.
781 The **MeasureObjectIntensity** module was then used to quantify intensity in nuclear and
782 perinuclear regions. SA-βgal+ associated nuclei were manually counted using Fiji
783 software (Schindelin et al. 2012). For all quantifications, Dunnett's test was used to test
784 for significance between pairwise comparisons of conditions.

785 **SA-βgal staining**

786 Senescence-associated beta galactosidase (SA-βgal) staining was conducted following
787 the manufacturer's protocol (Cat #9860S, Cell Signaling Technology), with all reagents
788 diluted in 1× PBS instead of dH2O.

789 **Colony formation assays**

790 Clonogenic outgrowth was performed in a 6-well plate by plating 1600, 800, and 400 cells
791 per well using a 2× serial dilution method. Cells were allowed to grow for 10-12 days in
792 drug-free media, followed by staining with crystal violet (1.25 g in 100 mL methanol and
793 400 mL distilled water) for 10 minutes at RT. Plates were scanned using an Epson
794 Perfection V600 photo scanner.

795 **Western blots**

796 Cells grown in a 10cm dish were washed once with ice-cold 1x Tris Buffer Saline (TBS),
797 then scraped into 2mL of ice-cold 1x TBS contained 1x phosSTOP (Cat #04906845001,

798 Millipore Sigma) & 1x cOmplete™ EDTA-free Protease Inhibitor (Cat #11836170001,
799 Millipore Sigma). Cells were spun down at 400g for 10 minutes at 4oC, before removing
800 the supernatant. 100-200 µL of 1x Laemmli buffer (Cat #1610747, Bio-Rad) + 50mM
801 Dithiothreitol (DTT) + 10% glycerol + 1x phosSTOP & 1x cOmplete™ EDTA-free Protease
802 Inhibitor was added to the cell pellet before boiling at 95°C for 5 minutes. Cell lysates
803 were then sonicated for 3 cycles of 10 seconds on and 25 seconds off on the Bioruptor.

804 4–20% Mini-PROTEAN® TGX™ Precast Protein Gels (Cat # 4561096, Bio-Rad) were
805 ran in 1x Tris/Glycine/SDS buffer (Cat #1610732) at 200V for 30 minutes then transferred
806 to a nitrocellulose membrane (Cytiva, 0.1 µm pore size, Cat #10600000) overnight at 4°C
807 in 1x transfer buffer [20 mM Tris, 150 mM Glycine, 20 % Methanol] (14V). Membranes
808 were blocked for 30 min at RT with Intercept® (TBS) Protein-Free Blocking Buffer (Cat#
809 927-80001, LICORbio), followed by primary antibody incubation (diluted in Intercept® T20
810 (TBS) Antibody diluent (Cat# 927-65001, LICORbio)) for overnight in 4°C. Membranes
811 were washed then incubated 1:10,000 dilution with secondary antibodies (Cat #926-
812 32211, Cat #926-68070, LICORbio) for 1 hour at RT and washed. Blots were then imaged
813 on a LI-COR Odyssey M system. Each wash step occurred 3x, 5 min each wash, in 1x
814 TBS + 0.05% Tween-20.

815 The following antibodies were used: Phospho-p53 (Ser15) Antibody (Cat #9284, Cell
816 Signaling Technologies) 1:1000, p53 Antibody Cat #9282) 1:1000, GAPDH (D4C6R)
817 Mouse Monoclonal Antibody, (Cat #97166, Cell Signaling Technologies), Phospho-Chk2
818 (Thr68) (C13C1) Rabbit Monoclonal Antibody (Cat #2197, Cell Signaling Technology)
819 1:1000, Chk2 (D9C6) Rabbit Monoclonal Antibody (Cat #6334, Cell Signaling Technology)
820 1:1000

821 Signal intensities of protein bands relative to loading control was quantified following the
822 ImageJ protocol described by (Davarin 2015).

823 **RNA-sequencing**

824 RNA extraction was done on at least 2 biological replicates per condition using the Quick-
825 RNA Microprep Kit (Cat #R1050, Zymo Research). Sample quality was checked by
826 determining RNA integrity number (RIN) via running samples through High Sensitivity
827 RNA ScreenTape (Cat #5067-5579, Agilent Technologies) on the Tapestation.
828 LS8817 cells: Samples were sent to Novogene for stranded library preparation and
829 sequencing. cDNA libraries were made with NEBNext® Ultra™ II Directional RNA Library
830 Prep Kit for Illumina (Cat #E7765, New England Biolabs) and sequenced on Illumina
831 NovaSeq 6000 Sequencing System as 150-base pair-end reads.

832 **ATAC-sequencing**

833 ATAC libraries were generated following Corces et al. protocol for OMNI-ATAC (Corces
834 et al. 2017). In brief, cells were treated in culture medium with DNase (Cat #LS002007,
835 Worthington) at a final concentration of 200 U/mL at 37 °C for 30 minutes, then washed
836 twice with PBS at 500 RCF, RT. Approximately ~50,000-60,000 cells were used for each
837 transposition reaction. Following permeabilization, 2.5 µL of Illumina TDE1 enzyme (Cat#
838 20034198, Illumina) was used for transposition at 37 °C for 30 minutes. Libraries were
839 PCR amplified for 8-13 cycles with Illumina i5 or i7 barcoded primers and were cleaned
840 up pre- and post-amplification following the manufacturer's instructions using Zymo DNA
841 Clean and Concentrator-5 Kit (Cat# D4014, Zymo Research). At least 2 technical
842 replicates and 2 biological replicates per condition were sequenced. Fragment length

843 distribution and DNA amount was quantified via TapeStation and Qubit to assess for
844 quality prior to sequencing. Libraries were sequenced on the Illumina NovaSeq 6000 or
845 on the NextSeq 1000 Sequencing System.

846 **CUT&Tag sequencing**

847 CUT&Tag on LS8817 cells was performed following the protocol from Kaya-Okur et al.
848 (Kaya-Okur et al. 2020) and was previously described in Soroczynski et al. (Soroczynski
849 et al. 2024). Antibodies used include: Anti-Histone H3 (acetyl K27) antibody - ChIP Grade
850 (ab4729, Abcam), 1:100; Guinea Pig anti-Rabbit IgG (Heavy & Light Chain) antibody
851 (ABIN101961, Antibodies-online), 1:100.

852 **CUT&RUN sequencing**

853 CUT&RUN in LS8817 cells was performed on macroH2A1 (Cat #ab37264, lot #1046297-
854 1, Abcam), 1:100 following an optimized protocol by Epicypher (Version 2.2). NEBNext
855 Ultra II DNA Library Prep Kit for Illumina was used for fragmentation, end repair and dA-
856 tailing, adapter ligation and PCR amplification according to the manufacturer's
857 instructions. Ampure XP beads were used for post-PCR cleanup. Samples were eluted in
858 IDTE buffer.

859 **RT-qPCR**

860 Total RNA was extracted using the Quick-RNA Microprep Kit (Cat# R1050, Zymo
861 Research) from at least two biological replicates per condition. cDNA was synthesized
862 with the Applied Biosystems High-Capacity cDNA Reverse Transcription Kit (Cat#

863 4368814, Thermo Fisher Scientific) and SUPERase• In™ RNase Inhibitor (Cat# AM2696,
864 Thermo Fisher Scientific). Prior to qPCR, cDNA was diluted to 5 ng/μL in dH2O.

865 qPCR was performed in triplicate in a 96-well microplate using a 15 μL reaction containing
866 7.5 μL PowerUp SYBR Green Master Mix (Cat# A25742, Thermo Fisher Scientific), 4 μL
867 dH2O, 0.75 μL each of forward and reverse primers, and 1.5 μL of 5 ng/μL cDNA.
868 Reactions were run on a QuantStudio™ 5 Real-Time PCR System with the following
869 untreated cycling conditions: 98°C for 30 seconds, followed by 40–45 cycles of 98°C for
870 10 seconds, 63°C for 30 seconds, and 72°C for 1 minute. Cq values were normalized to
871 the housekeeping gene *PUM1*, which was selected based on its stable expression across
872 conditions in RNA-seq datasets.

873 All sequencing datasets have been deposited in the Gene Expression Omnibus (GEO)
874 database. Code supporting analysis of sequencing datasets can be found at
875 https://github.com/yeungj234/Manuscript_Figures. Further information and request for
876 resources and reagents should be directed to and will be fulfilled by the lead contact, Dr.
877 Viviana Risca (vrisca@rockefeller.edu).

878 ATACseq: GSE295258 (Reviewer token: ojihqayqnhethgj)
879 RNA-seq: GSE295260 (Reviewer token: qbsxqqouzxufzub)
880 CUT&Tag: GSE295261 (Reviewer token: shapgsuwfnqthcp)

881 **COMPETING INTERESTS STATEMENT**

882 V. I. R. has submitted a patent application (PCT/US2024/059554) for a chromatin
883 conformation capture method.

ACKNOWLEDGMENTS

J. L. Y. acknowledges support from a Natural Sciences and Engineering Research Council of Canada Postgraduate Scholarships – Doctoral scholarship. J. R. was supported by the American Cancer Society – Fairfield Research Council– Postdoctoral Fellowship, PF-23-1034949-01-CCB, https://doi.org/10.53354/ACS.PF-23-1034949-01-CCB.pc.gr.168157. L. A. W. acknowledges support from the NSF Graduate Research Fellowship Program (1946429). This work was supported in part by a V Scholar Award (V2019-011) from the V Foundation for Cancer Research, by a Starr Cancer Consortium Grant (I16-0058), a Scholar Award from The Rita Allen Foundation (S-2108-02147), and a Career Scientist Award from the Irma T. Hirschl/Monique Weill-Caulier Trust.

We acknowledge support from the Rockefeller University Genomics Resource Center (RRID:SCR_020986), and the High-Performance Computing Resource Center (RRID:SCR_025889). We thank Andrew Koff for providing us with the LS8817 cell line and for scientific insights. We thank Andrew Scortea for administrative support and his work in setting up the Risca laboratory. We thank Wei Zhou and Rochelle Shih for technical assistance. We thank all members of the Risca and Koff laboratories, Hironori Funabiki, Lydia Finley and Junyue Cao for insightful discussions and advice.

AUTHOR CONTRIBUTIONS

J. L. Y.: Conceptualization of project, performed experiments, data analysis, visualization and curation, manuscript writing and editing. J. R.: Performed experiments, data analysis, manuscript writing and editing, and provided mentorship. N. P.: Bioinformatics analysis. L. A. W..: Performed experiments, image analysis and manuscript editing. A. O.: Performed experiments. M. P.: Performed experiments and manuscript editing. I. D.:

Bioinformatics analysis. R. H.: Bioinformatics analysis. B. T.: Performed experiments and image analysis. V. I. R.: Conceptualization of project, resources, project supervision, mentorship, funding acquisition, manuscript writing and editing.

REFERENCES

Acosta JC, Gil J. 2009. A role for CXCR2 in senescence, but what about in cancer? *Cancer Res* **69**: 2167–2170.

Aird KM, Iwasaki O, Kossenkov AV, Tanizawa H, Fatkhutdinov N, Bitler BG, Le L, Alicea G, Yang TL, Johnson FB et al. 2016. HMGB2 orchestrates the chromatin landscape of senescence-associated secretory phenotype gene loci. *J Cell Biol* **215**: 325–334.

Ajoolabady A, Pratico D, Bahijri S, Tuomilehto J, Uversky VN, Ren J. 2025. Hallmarks of cellular senescence: biology, mechanisms, regulations. *Exp Mol Med* **57**: 1482–1491.

Ancrile B, Lim KH, Counter CM. 2007. Oncogenic Ras-induced secretion of IL6 is required for tumorigenesis. *Genes Dev* **21**: 1714–1719.

Awasthi N, Liongue C, Ward AC. 2021. STAT proteins: a kaleidoscope of canonical and non-canonical functions in immunity and cancer. *J Hematol Oncol* **14**: 198.

Balamurugan K, Sterneck E. 2013. The many faces of C/EBPδ and their relevance for inflammation and cancer. *Int J Biol Sci* **9**: 917–933.

Barretina J, Taylor BS, Banerji S, Ramos AH, Lagos-Quintana M, Decarolis PL, Shah K, Socci ND, Weir BA, Ho A et al. 2010. Subtype-specific genomic alterations define new targets for soft-tissue sarcoma therapy. *Nat Genet* **42**: 715–721.

Basisty N, Kale A, Jeon OH, Kuehnemann C, Payne T, Rao C, Holtz A, Shah S, Sharma V, Ferrucci L et al. 2020. A proteomic atlas of senescence-associated secretomes for aging biomarker development. *PLoS Biol* **18**: e3000599.

Biddie SC, John S, Sabo PJ, Thurman RE, Johnson TA, Schiltz RL, Miranda TB, Sung MH, Trump S, Lightman SL et al. 2011. Transcription factor AP1 potentiates chromatin accessibility and glucocorticoid receptor binding. *Mol Cell* **43**: 145–155.

Bournique E, Sanchez A, Oh S, Ghazarian D, Mahieu AL, Manjunath L, Ednacot E, Ortega P, Masri S, Marazzi I et al. 2025. ATM and IRAK1 orchestrate two distinct mechanisms of NF-kappaB activation in response to DNA damage. *Nat Struct Mol Biol* **32**: 740–755.

Brill E, Gobble R, Angeles C, Lagos-Quintana M, Crago A, Laxa B, Decarolis P, Zhang L, Antonescu C, Socci ND et al. 2010. ZIC1 overexpression is oncogenic in liposarcoma. *Cancer Res* **70**: 6891–6901.

Chen H, Ruiz PD, McKimpson WM, Novikov L, Kitsis RN, Gamble MJ. 2015. MacroH2A1 and ATM Play Opposing Roles in Paracrine Senescence and the Senescence-Associated Secretory Phenotype. *Mol Cell* **59**: 719–731.

Chien Y, Scuoppo C, Wang X, Fang X, Balgley B, Bolden JE, Premsrirut P, Luo W, Chicas A, Lee CS et al. 2011a. Control of the senescence-associated secretory phenotype by NF-kappaB promotes senescence and enhances chemosensitivity. *Genes Dev* **25**: 2125–2136.

Corces MR, Trevino AE, Hamilton EG, Greenside PG, Sinnott-Armstrong NA, Vesuna S, Satpathy AT, Rubin AJ, Montine KS, Wu B et al. 2017. An improved ATAC-seq protocol reduces background and enables interrogation of frozen tissues. *Nat Methods* **14**: 959–962.

Crago AM, Singer S. 2011. Clinical and molecular approaches to well differentiated and dedifferentiated liposarcoma. *Curr Opin Oncol* **23**: 373–378.

Creytens D, Van Gorp J, Speel EJ, Ferdinande L. 2015. Characterization of the 12q amplicons in lipomatous soft tissue tumors by multiplex ligation-dependent probe amplification-based copy number analysis. *Anticancer Res* **35**: 1835–1842.

Croston GE, Cao Z, Goeddel DV. 1995. NF-kappa B activation by interleukin-1 (IL-1) requires an IL-1 receptor-associated protein kinase activity. *J Biol Chem* **270**: 16514–16517.

Currey L, Thor S, Piper M. 2021. TEAD family transcription factors in development and disease. *Development* **148**.

Davarin H. 2015. Quantifications of Western Blots with ImageJ. York University.

Dickson MA, Schwartz GK, Keohan ML, D'Angelo SP, Gounder MM, Chi P, Antonescu CR, Landa J, Qin LX, Crago AM et al. 2016. Progression-Free Survival Among Patients With Well-Differentiated or Dedifferentiated Liposarcoma Treated With CDK4 Inhibitor Palbociclib: A Phase 2 Clinical Trial. *JAMA Oncol* **2**: 937–940.

Freudlsperger C, Bian Y, Contag Wise S, Burnett J, Coupar J, Yang X, Chen Z, Van Waes C. 2013. TGF-beta and NF-kappaB signal pathway cross-talk is mediated through TAK1 and SMAD7 in a subset of head and neck cancers. *Oncogene* **32**: 1549–1559.

Fujioka S, Niu J, Schmidt C, Sclabas GM, Peng B, Uwagawa T, Li Z, Evans DB, Abbruzzese JL, Chiao PJ. 2004. NF-kappaB and AP-1 connection: mechanism of NF-kappaB-dependent regulation of AP-1 activity. *Mol Cell Biol* **24**: 7806–7819.

Garlanda C, Mantovani A. 2021. Interleukin-1 in tumor progression, therapy, and prevention. *Cancer Cell* **39**: 1023–1027.

Gleason CE, Dickson MA, Klein Dooley ME, Antonescu CR, Gularte-Merida R, Benitez M, Delgado JI, Kataru RP, Tan MWY, Bradic M et al. 2024. Therapy-Induced Senescence Contributes to the Efficacy of Abemaciclib in Patients with Dedifferentiated Liposarcoma. *Clin Cancer Res* **30**: 703–718.

Gobble RM, Qin LX, Brill ER, Angeles CV, Ugras S, O'Connor RB, Moraco NH, Decarolis PL, Antonescu C, Singer S. 2011. Expression profiling of liposarcoma yields a multigene predictor of patient outcome and identifies genes that contribute to liposarcomagenesis. *Cancer Res* **71**: 2697–2705.

Goel S, DeCristo MJ, Watt AC, BrinJones H, Sceneay J, Li BB, Khan N, Ubellacker JM, Xie S, Metzger-Filho O et al. 2017. CDK4/6 inhibition triggers anti-tumour immunity. *Nature* **548**: 471–475.

Golson ML, Kaestner KH. 2016. Fox transcription factors: from development to disease. *Development* **143**: 4558–4570.

Guan X, LaPak KM, Hennessey RC, Yu CY, Shakya R, Zhang J, Burd CE. 2017. Stromal Senescence By Prolonged CDK4/6 Inhibition Potentiates Tumor Growth. *Mol Cancer Res* **15**: 237–249.

Guo Q, Jin Y, Chen X, Ye X, Shen X, Lin M, Zeng C, Zhou T, Zhang J. 2024. NF-kappaB in biology and targeted therapy: new insights and translational implications. *Signal Transduct Target Ther* **9**: 53.

Han CY, Kang I, Harten IA, Gebe JA, Chan CK, Omer M, Alonge KM, den Hartigh LJ, Gomes Kjerulf D, Goodspeed L et al. 2020. Adipocyte-Derived Versican and Macrophage-Derived Biglycan Control Adipose Tissue Inflammation in Obesity. *Cell Rep* **31**: 107818.

Hernandez-Segura A, Nehme J, Demaria M. 2018. Hallmarks of Cellular Senescence. *Trends Cell Biol* **28**: 436–453.

Huh HD, Kim DH, Jeong HS, Park HW. 2019. Regulation of TEAD Transcription Factors in Cancer Biology. *Cells* **8**.

Ji Z, He L, Regev A, Struhl K. 2019. Inflammatory regulatory network mediated by the joint action of NF-kB, STAT3, and AP-1 factors is involved in many human cancers. *Proc Natl Acad Sci U S A* **116**: 9453–9462.

Jones SA, Jenkins BJ. 2018. Recent insights into targeting the IL-6 cytokine family in inflammatory diseases and cancer. *Nat Rev Immunol* **18**: 773–789.

Kamachi Y, Kondoh H. 2013. Sox proteins: regulators of cell fate specification and differentiation. *Development* **140**: 4129–4144.

Kaya-Okur HS, Janssens DH, Henikoff JG, Ahmad K, Henikoff S. 2020. Efficient low-cost chromatin profiling with CUT&Tag. *Nat Protoc* **15**: 3264–3283.

Kelsh RM, McKeown-Longo PJ. 2013. Topographical changes in extracellular matrix: Activation of TLR4 signaling and solid tumor progression. *Trends Cancer Res* **9**: 1–13.

Klein ME, Kovatcheva M, Davis LE, Tap WD, Koff A. 2018. CDK4/6 Inhibitors: The Mechanism of Action May Not Be as Simple as Once Thought. *Cancer Cell* **34**: 9–20.

Kovatcheva M, Liao W, Klein ME, Robine N, Geiger H, Crago AM, Dickson MA, Tap WD, Singer S, Koff A. 2017. ATRX is a regulator of therapy induced senescence in human cells. *Nat Commun* **8**: 386.

Kovatcheva M, Liu DD, Dickson MA, Klein ME, O'Connor R, Wilder FO, Socci ND, Tap WD, Schwartz GK, Singer S et al. 2015. MDM2 turnover and expression of ATRX determine the choice between quiescence and senescence in response to CDK4 inhibition. *Oncotarget* **6**: 8226–8243.

Lau L, David G. 2019. Pro- and anti-tumorigenic functions of the senescence-associated secretory phenotype. *Expert Opin Ther Targets* **23**: 1041–1051.

Lee DH, Imran M, Choi JH, Park YJ, Kim YH, Min S, Park TJ, Choi YW. 2024. CDK4/6 inhibitors induce breast cancer senescence with enhanced anti-tumor immunogenic properties compared with DNA-damaging agents. *Mol Oncol* **18**: 216–232.

Lee S, Schmitt CA. 2019. The dynamic nature of senescence in cancer. *Nat Cell Biol* **21**: 94–101.

Li YJ, Zhang C, Martincuks A, Herrmann A, Yu H. 2023. STAT proteins in cancer: orchestration of metabolism. *Nat Rev Cancer* **23**: 115–134.

Loughery J, Cox M, Smith LM, Meek DW. 2014. Critical role for p53-serine 15 phosphorylation in stimulating transactivation at p53-responsive promoters. *Nucleic Acids Res* **42**: 7666–7680.

Makulyte G, Safwan-Zaiter H, Goehrig D, Huna A, Mangelinck A, Mikawa T, Palazzo A, Moudombi L, Medard JJ, Chanal M et al. 2026. The Proinflammatory Secretome of Senescent Cells Can Be Controlled by a HIF2A-Dependent Upregulation and a FURIN-Dependent Cleavage of the ANGPTL4 Secreted Factor. *Aging Cell* **25**: e70307.

Malaquin N, Martinez A, Rodier F. 2016. Keeping the senescence secretome under control: Molecular reins on the senescence-associated secretory phenotype. *Exp Gerontol* **82**: 39–49.
Martínez-Zamudio RI, Roux PF, de Freitas JANL, Robinson L, Doré G, Sun B, Belenki D, Milanovic M, Herbig U, Schmitt CA et al. 2020. AP-1 imprints a reversible transcriptional programme of senescent cells. *Nat Cell Biol* **22**: 842–855.
McHugh D, Gil J. 2018. Senescence and aging: Causes, consequences, and therapeutic avenues. *J Cell Biol* **217**: 65–77.
Miller ML, Molinelli EJ, Nair JS, Sheikh T, Samy R, Jing X, He Q, Korkut A, Crago AM, Singer S et al. 2013. Drug synergy screen and network modeling in dedifferentiated liposarcoma identifies CDK4 and IGF1R as synergistic drug targets. *Sci Signal* **6**: ra85.
Miyamoto S. 2011. Nuclear initiated NF-kappaB signaling: NEMO and ATM take center stage. *Cell Res* **21**: 116–130.
Narita M, Nunez S, Heard E, Narita M, Lin AW, Hearn SA, Spector DL, Hannon GJ, Lowe SW. 2003. Rb-mediated heterochromatin formation and silencing of E2F target genes during cellular senescence. *Cell* **113**: 703–716.
Oeckinghaus A, Hayden MS, Ghosh S. 2011. Crosstalk in NF-kappaB signaling pathways. *Nat Immunol* **12**: 695–708.
Patrick R, Naval-Sanchez M, Deshpande N, Huang Y, Zhang J, Chen X, Yang Y, Tiwari K, Esmaeili M, Tran M et al. 2024. The activity of early-life gene regulatory elements is hijacked in aging through pervasive AP-1-linked chromatin opening. *Cell Metab* **36**: 1858–1881 e1823.
Pazolli E, Alspach E, Milczarek A, Prior J, Piwnica-Worms D, Stewart SA. 2012. Chromatin remodeling underlies the senescence-associated secretory phenotype of tumor stromal fibroblasts that supports cancer progression. *Cancer Res* **72**: 2251–2261.
Pierce JW, Schoenleber R, Jesmok G, Best J, Moore SA, Collins T, Gerritsen ME. 1997. Novel inhibitors of cytokine-induced IkappaBalpha phosphorylation and endothelial cell adhesion molecule expression show anti-inflammatory effects in vivo. *J Biol Chem* **272**: 21096–21103.
Pospelova TV, Demidenko ZN, Bukreeva EI, Pospelov VA, Gudkov AV, Blagosklonny MV. 2009. Pseudo-DNA damage response in senescent cells. *Cell Cycle* **8**: 4112–4118.
Rebe C, Ghiringhelli F. 2020. Interleukin-1beta and Cancer. *Cancers (Basel)* **12**.
Ren Q, Liu Z, Wu L, Yin G, Xie X, Kong W, Zhou J, Liu S. 2023. C/EBPβ: The structure, regulation, and its roles in inflammation-related diseases. *Biomed Pharmacother* **169**: 115938.
Rodier F, Coppe JP, Patil CK, Hoeijmakers WA, Munoz DP, Raza SR, Freund A, Campeau E, Davalos AR, Campisi J. 2009. Persistent DNA damage signalling triggers senescence-associated inflammatory cytokine secretion. *Nat Cell Biol* **11**: 973–979.
Romano O, Miccio A. 2020. GATA factor transcriptional activity: Insights from genome-wide binding profiles. *IUBMB Life* **72**: 10–26.
Saito S, Goodarzi AA, Higashimoto Y, Noda Y, Lees-Miller SP, Appella E, Anderson CW. 2002. ATM mediates phosphorylation at multiple p53 sites, including Ser(46), in response to ionizing radiation. *J Biol Chem* **277**: 12491–12494.

Sakaguchi K, Herrera JE, Saito S, Miki T, Bustin M, Vassilev A, Anderson CW, Appella E. 1998. DNA damage activates p53 through a phosphorylation-acetylation cascade. *Genes Dev* **12**: 2831–2841.

Salminen A, Kauppinen A, Kaarniranta K. 2012. Emerging role of NF-kappaB signaling in the induction of senescence-associated secretory phenotype (SASP). *Cell Signal* **24**: 835–845.

Sarkar A, Hochedlinger K. 2013. The sox family of transcription factors: versatile regulators of stem and progenitor cell fate. *Cell Stem Cell* **12**: 15–30.

Schindelin J, Arganda-Carreras I, Frise E, Kaynig V, Longair M, Pietzsch T, Preibisch S, Rueden C, Saalfeld S, Schmid B et al. 2012. Fiji: an open-source platform for biological-image analysis. *Nat Methods* **9**: 676–682.

Schmitt CA, Wang B, Demaria M. 2022. Senescence and cancer - role and therapeutic opportunities. *Nat Rev Clin Oncol* **19**: 619–636.

Singer S, Socci ND, Ambrosini G, Sambol E, Decarolis P, Wu Y, O'Connor R, Maki R, Viale A, Sander C et al. 2007. Gene expression profiling of liposarcoma identifies distinct biological types/subtypes and potential therapeutic targets in well-differentiated and dedifferentiated liposarcoma. *Cancer Res* **67**: 6626–6636.

Soroczynski J, Anderson LJ, Yeung JL, Rendleman JM, Oren DA, Konishi HA, Risca VI. 2024. OpenTn5: Open-Source Resource for Robust and Scalable Tn5 Transposase Purification and Characterization. *bioRxiv*.

Stirling DR, Swain-Bowden MJ, Lucas AM, Carpenter AE, Cimini BA, Goodman A. 2021. CellProfiler 4: improvements in speed, utility and usability. *BMC Bioinformatics* **22**: 433.

Sun Z, Filipescu D, Andrade J, Gaspar-Maia A, Ueberheide B, Bernstein E. 2018. Transcription-associated histone pruning demarcates macroH2A chromatin domains. *Nat Struct Mol Biol* **25**: 958–970.

Tremblay M, Sanchez-Ferras O, Bouchard M. 2018. GATA transcription factors in development and disease. *Development* **145**.

Vierbuchen T, Ling E, Cowley CJ, Couch CH, Wang X, Harmin DA, Roberts CWM, Greenberg ME. 2017. AP-1 Transcription Factors and the BAF Complex Mediate Signal-Dependent Enhancer Selection. *Mol Cell* **68**: 1067–1082 e1012.

Wagner V, Gil J. 2020. Senescence as a therapeutically relevant response to CDK4/6 inhibitors. *Oncogene* **39**: 5165–5176.

Wang B, Han J, Elisseeff JH, Demaria M. 2024. The senescence-associated secretory phenotype and its physiological and pathological implications. *Nat Rev Mol Cell Biol* **25**: 958–978.

Wang B, Kohli J, Demaria M. 2020. Senescent Cells in Cancer Therapy: Friends or Foes? *Trends Cancer* **6**: 838–857.

Wang B, Varela-Eirin M, Brandenburg SM, Hernandez-Segura A, van Vliet T, Jongbloed EM, Wilting SM, Ohtani N, Jager A, Demaria M. 2022. Pharmacological CDK4/6 inhibition reveals a p53-dependent senescent state with restricted toxicity. *EMBO J* **41**: e108946.

Wang W, Gao W, Zhu Q, Alasbahi A, Seki E, Yang L. 2021. TAK1: A Molecular Link Between Liver Inflammation, Fibrosis, Steatosis, and Carcinogenesis. *Front Cell Dev Biol* **9**: 734749.

Watt AC, Cejas P, DeCristo MJ, Metzger-Filho O, Lam EYN, Qiu X, BrinJones H, Kesten N, Coulson R, Font-Tello A et al. 2021. CDK4/6 inhibition reprograms the breast cancer enhancer landscape by stimulating AP-1 transcriptional activity. *Nat Cancer* **2**: 34–48.

Weber A, Wasiliew P, Kracht M. 2010. Interleukin-1 (IL-1) pathway. *Sci Signal* **3**: cm1.

Wesche H, Korherr C, Kracht M, Falk W, Resch K, Martin MU. 1997. The interleukin-1 receptor accessory protein (IL-1RAcP) is essential for IL-1-induced activation of interleukin-1 receptor-associated kinase (IRAK) and stress-activated protein kinases (SAP kinases). *J Biol Chem* **272**: 7727–7731.

Wiley CD, Velarde MC, Lecot P, Liu S, Sarnoski EA, Freund A, Shirakawa K, Lim HW, Davis SS, Ramanathan A et al. 2016. Mitochondrial Dysfunction Induces Senescence with a Distinct Secretory Phenotype. *Cell Metab* **23**: 303–314.

Wu T, Yang W, Sun A, Wei Z, Lin Q. 2022. The Role of CXC Chemokines in Cancer Progression. *Cancers (Basel)* **15**.

Zhang R, Chen W, Adams PD. 2007. Molecular dissection of formation of senescence-associated heterochromatin foci. *Mol Cell Biol* **27**: 2343–2358.

Zhang R, Poustovoitov MV, Ye X, Santos HA, Chen W, Daganzo SM, Erzberger JP, Serebriiskii IG, Canutescu AA, Dunbrack RL et al. 2005. Formation of MacroH2A-containing senescence-associated heterochromatin foci and senescence driven by ASF1a and HIRA. *Dev Cell* **8**: 19–30.